



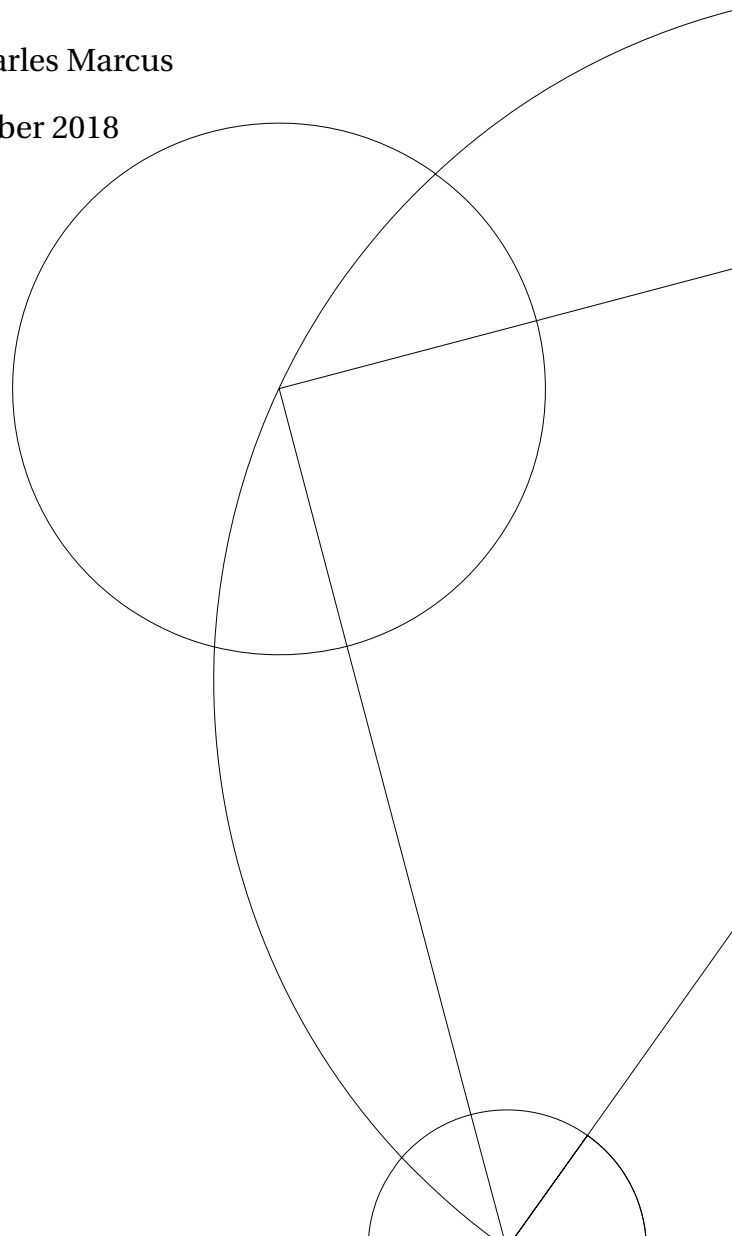
# Probing correlations and nonlocal conductance in Majorana wires

Gian-Luca Romano Anselmetti

znq301@alumni.ku.dk

Supervisor: Charles Marcus

3rd September 2018





## **Acknowledgements**

First and foremost I would like to thank head of department Charles Marcus for supervision and letting me spend an exciting year in this research group. I learned a lot on what it means to be an experimental physicist and what mindset one should keep when pushing boundaries. Further my thanks goes to Saulius Vaitiekėnas for teaching me the fine arts of fabrication, documentation and measurement, Andrew Higginbotham for detailed discussions about operation amplifiers and guidance through the jungle of bound states, Lucas Casparis for the pondering over measurement data and to have an ear for my various fabrication related miseries and Gerbold Menard for a big help with measurement and my data analysis work. My thanks also goes to Shivendra Upadhyay and the fabrication staff for every help in development of new recipes on new material I received.

My family and friends shall not go unmentioned as I owe them a lot for their unconditional love, help, strength and keeping my mood up in times of shattered III-V chips/hopes. This work would not exist in the way it does without all of you.



## Abstract

The possibility of topological quantum computation based on the braiding of Majorana zero modes has been a topic of interest for the last decade, both in industry and in science. Being more of a playground for theoreticians at first, breakthroughs in material sciences allowed for hybrid systems with high spin-orbit interaction, large Landé  $g$ -factors and induced superconductivity to be created. By bringing these properties together at millikelvin temperatures with applied parallel magnetic field, signatures such as the *zero bias peak* have been observed in nanowires and two dimensional electron gases independently. This hints at a degenerate ground state at zero energy, one of two major properties of non-abelian anyons constituted for these braiding operations. All promising steps towards engineering a semiconducting system to host a topological qubit.

The work presented extends the recent development on selective area grown structures by molecular beam epitaxy and chemical beam epitaxy as a new platform for Majorana zero modes. By extending the two terminal wire geometry of epitaxially grown nanowires this work develops a measurement set-up to record a full picture of the conductances in a three terminal device consisting of a proximitized InAs nanowire contacted by two normal leads and one superconducting lead. Careful estimates of the effect of voltage division effects on a three terminal measurements are studied and integrated in the measurement setup. Via simultaneous two-sided spectroscopy we find correlations in energy spacing and couplings of Andreev bound states over the extend of 300nm and compare these with measurements on a device with 900nm extent between the tunneling probes. Furthermore we observe correlated signatures of positive and negative differential conductance in the nonlocal conductances during these measurements, investigate their behavior under gate and magnetic field changes and provide some interpretation in how they come to be. In another device of 1  $\mu\text{m}$  length we observe the first zero bias conductance peak on this platform on one side and discuss the implications of this measurement.



# Contents

<b>1</b>	<b>Introduction</b>	<b>1</b>
<b>2</b>	<b>Computation - Quo vadis?</b>	<b>1</b>
2.1	Quantum computation . . . . .	2
2.2	Topology and topological quantum computation . . . . .	3
<b>3</b>	<b>Topology in Condensed Matter</b>	<b>6</b>
3.1	Superconductivity . . . . .	6
3.2	Andreev reflection . . . . .	7
3.3	Superconducting proximity effect . . . . .	8
3.4	Andreev bound states . . . . .	9
3.4.1	Andreev bound states with charging energy . . . . .	10
3.4.2	ABS in a three terminal measurement . . . . .	11
3.5	1D Kitaev Chain . . . . .	14
3.6	Engineering Majorana fermions in nanowires . . . . .	16
<b>4</b>	<b>A new platform for topological quantum computation</b>	<b>18</b>
4.1	Signs of Majorana bound states in nanowires . . . . .	18
4.2	Selective area growth . . . . .	19
<b>5</b>	<b>Measurement and Fabrication</b>	<b>21</b>
5.1	Dilution refrigerator . . . . .	21
5.2	Lithography . . . . .	22
5.3	Wet etch . . . . .	23
5.4	Device Fabrication . . . . .	25
5.4.1	Step 0: Design preparation and other prefabrication steps . . . . .	25
5.4.2	Step 1: Aluminum etch . . . . .	26
5.4.3	Step 2: Titanium-Gold contacts . . . . .	27
5.4.4	Step 3: Oxide layer . . . . .	27
5.4.5	Step 4: Titanium-Gold gates . . . . .	28
5.5	Measurement setup . . . . .	29
5.5.1	Two vs. three terminal measurement . . . . .	29
5.5.2	Voltage divider . . . . .	30
5.5.3	Measurement Setup . . . . .	31
5.5.4	Noise reduction . . . . .	32
<b>6</b>	<b>Results</b>	<b>34</b>
6.1	Tuning into the double tunneling regime . . . . .	34
6.2	Two sided tunneling spectroscopy . . . . .	38
6.3	Nonlocal conductances . . . . .	42
6.4	Field dependence . . . . .	44
6.5	Possible Majorana zero modes . . . . .	46

<b>7 Conclusion and Outlook</b>	<b>49</b>
7.1 Conclusion . . . . .	49
7.2 Outlook . . . . .	50
<b>A Single bias vs. dual biasing</b>	<b>56</b>
<b>B Voltage division effects</b>	<b>57</b>
B.1 Floating third lead . . . . .	57
B.2 Differential conductance vs. derivated conductance . . . . .	58
B.3 Frequency swap and all measured conductances . . . . .	59

## 1 Introduction

This work has the ambition to provide a reader with limited knowledge about quantum computation a good introduction while still being detailed for the more informed audience. Its structure is a causal chain which leads from today's computers to the research done in the past year. We start off by evaluating where the field of computation itself stands in the present day and which challenges it faces currently. Leading from these challenges, we briefly introduce the ideas and advantages of quantum computation over classical computation and more specifically topological quantum computation. After this, elementary concepts in condensed matter are introduced to understand the bound states and possible topological excitations in our probed systems. This is followed by recent findings of Majorana zero modes in semiconducting systems and the development of the new platform of selective area grown (SAG) structures which promises scalability and the realization of more sophisticated architectures. Spending some time on measurement methods and device fabrication, I report on findings in this new generation of semiconductor-superconductor hybrid devices. As detailed derivations of many of these effects are beyond the scope of this thesis, the interested reader is provided with additional resources at the relevant places which go into more detail.

## 2 Computation - Quo vadis?

The ability to compute, transfer and store information digitally has transformed our world like few technologies have before and has been a catalyst for development in all other branches of science. The basis of all classical computation is the *bit*, which can be in either an on or off state. In this binary mathematical bases it is possible to reduce all higher order calculations to a basis set of operations: In classical computation every mathematical operation can be constructed for example out of either an AND or OR and the NOT operation.

When talking about computers and computation in general, it is important to keep in mind the separation of the mathematics of the computation and algorithms and the physical representation of the machine doing the calculation. In theory all classical computation could be done on a set of coins with heads and tails and the ambition to flip them over often enough following known algorithms and one could calculate everything modern computers can do today<sup>1</sup>.

The most common used piece of technology in classical computation has been the metal-oxide-semiconductor field-effect transistor (*MOSFET*)[1], a physical switch which toggles current running through a depletable region of doped silicon. Based on this technology, industry has progressed at an exponential rate postulated by Moore's law in 1965 [2]. There are different interpretations of this law, the original law stated that the number of integrated transistors on a given area of a chip will double every two years, a more modern version argues with the number of calculations per second per cost. All of these interpretations have slowed down from their exponential curve in the last decade[3]. The scale of the transistors is reaching a lower limit which is governed by the laws of quan-

---

<sup>1</sup>Obviously ignoring timescales in this example

tum mechanics. Below this limit electrons start to exhibit more and more of their quantum nature and e.g. start to have a non-zero probability of appearing on the other side of classically completely opaque barriers, a process referred to as quantum tunneling. Their wave-particle duality has to be considered and a full description has to treat them as a *wavefunction*. These quantum effects which lead to calculation errors in the classical picture open up a new way of calculation, which for certain problems promises a significant improvement in speed - quantum computation.

## 2.1 Quantum computation

After asking himself the question whether computers could effectively simulate any physical system, Richard Feynman gave birth to the idea of a computer which would be based on different mathematical principles that would allow for the simulation of quantum systems [4]. The reasoning behind it is quite simple - as soon as your simulated system allows for superposition of states the number of classical bits needed to represent all possible configurations of your system scales up exponentially and to store every configuration of 80 two-level-system the needed disk space is already bigger than the entirety of today's Internet. In our previously constructed toy model of visualizing bits as coins, a superposition can be thought of a spinning coin which has yet to fall on heads or tails. After the birth of this idea, more applications than just the simulation of quantum systems in this new mathematical bases were discovered. First, trivial mathematical problems (Deutsch [5]) showed that quantum computation could outperform classical methods but later more effective factorization of large numbers (Shor [6]) and faster database searches (Grover [7]) sparked interest in this technology.

The building block of a general quantum computer - the qubit

$$a |0\rangle + b |1\rangle \tag{1}$$

represents any state of the two-level system, with  $a$  and  $b$  as coefficients with  $\sqrt{a^2 + b^2} = 1$  and  $|0\rangle, |1\rangle$  being the eigenstates of your system, often also notated as  $|\uparrow\rangle, |\downarrow\rangle$ , depending on the choice of your system. All qubits are initialized in a known state, followed by the manipulation by applying Hermitian operators. Similar to classical computation there exists a basis set of operation to construct all other operations needed for universal quantum computing out of: the Hadamard-operation, which maps the eigenstates  $|0\rangle, |1\rangle$  on to their full superposition  $\frac{1}{\sqrt{2}} |0\rangle + \frac{1}{\sqrt{2}} |1\rangle, \frac{1}{\sqrt{2}} |0\rangle - \frac{1}{\sqrt{2}} |1\rangle$  and the CNOT operation, which negates the state of a qubit depending on the state of another qubit. After manipulation the final result of the operation has to be read out.

Because not every two-level system was created equal, in 2000 David DiVincenzo stated five criteria [8] necessary to implement a quantum computer, essentially covering the mentioned scheme above. The time in which all operation has to be finalized and read out is bounded by the third and maybe most challenging criterion - the decoherence time. Because decoherence directly influences the error rate of your system, it is necessary to isolate your qubits to avoid disturbance from the surrounding environment. Environmental noise leads to a small change in energy separation of your two level system. Following Schrödingers equation, the phase of all states evolves in time by rotating in phase space

depending on their respective energy. Small differences in energy of the excited states of two coupled qubits thus lead to a phase difference in time - they *dephase*. Below an error rate of  $10^{-3}$  it is possible to account for these errors with quantum error correction. Quantum error correction extends the global wavefunction on an additional set of qubits by quantum entanglement allowing for detection of local errors without collapsing the global wavefunction upon measurement [9, 10]. The size of this subset of qubits is dependent on the error rate of your qubits so a significant amount of your total qubits are only used for error correction and can't participate in the calculation itself. Some voices are being heard that it could be impossible to actively correct the decohering wavefunction of a system with a significant amount of qubits. A coupled system decoheres with  $1/N$  times the decoherence time of a single qubit where  $N$  is the number of qubits in this system [11]. This is the reason that a system which is inherently immune to noise (or at least a specific kind of noise) has a big advantage in terms of scalability and feasibility. One way to achieve partial immunity is a *transmon* [12], a superconducting qubit which is tuned to be in a regime where the Josephson energy  $E_J$  is much bigger than the charging energy  $E_C$  which reduces its sensitivity to charge noise. Another way is to be discussed in the following chapters and is the foundation on which this thesis is based on.

## 2.2 Topology and topological quantum computation

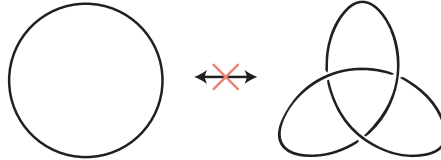


Figure 2.1: The trivial unknot in direct relation to the left-handed trefoil knot of first topological order. No continuous transformation mapping of one onto the other exists.

Topology is a branch of mathematics that deals with the continuous deformations of objects. This defines certain classes of objects which are ambiguous under these deformations but exclusive to their respective classes. In more layman terms, this means that every object of each class can be continuously transformed into each of the other objects of its class but not into any of another class. A visually clear example stems from the mathematical branch of knot theory. The simplest mathematical knot is the unknot, which is no knot at all (see Figure 2.1). Comparing it with the trefoil knot, the first non-trivial knot, it becomes clear that no continuous transformation of the former allows to arrive at the latter - they are of different topological order.

In physics, topology is concerned with the continuous transformation of two Hamiltonians into each other. If there exists a transformation mapping between the two, certain properties referred to as *topological invariants* are protected under these perturbations [13]. Topology in physics is a recent development, popularized by the Nobel price winning

discovery of the Kosterlitz-Thouless phase transition in a 2D system, which is a phase transition of infinite order [14]. It is explained by the formation of vortices and antivortices, topological excitations of your system, which pair up under given circumstances to save energy. It lead to the development of a number of topological effects like topological insulators [15, 16] and Majorana fermions [17] which can be used to achieve topological quantum computation.

To understand the foundation of topological quantum computing we have to introduce some quantum particle statistics. Particles are classified into two categories of *bosons* and *fermions*, that differ by there exchange statistics. Bosons are described by a symmetric wave function, exchanging two particles does not change the sign of the wave function. Fermions carry an antisymmetric wave function, meaning that exchanging two fermions leads to a sign change of the wave function which corresponds to a phase shift of  $\pi$ . In both cases, exchanging two particles twice returns the original wave function.

$$\text{Bosons: } |\Phi(x, y)\rangle \Rightarrow |\Phi(y, x)\rangle \quad (2)$$

$$\text{Fermions: } |\Phi(x, y)\rangle \Rightarrow -|\Phi(y, x)\rangle \quad (3)$$

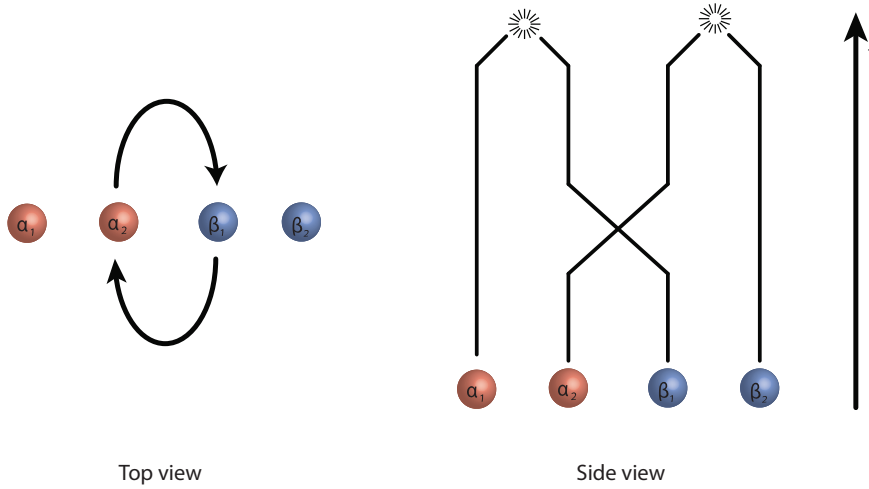


Figure 2.2: The view of the exchange of two non-abelian anyons in real space and following their worldlines in space time. Anyons are fused at the end of the operation to read out the state of the system.

In reduced dimensions, quasiparticles in the form of excitations called anyons can exhibit different exchange statistics. On one hand, there are the more common abelian anyons, which can carry a phase change between 0 and  $\pi$  upon exchange. On the other hand there is the proposal of non-abelian anyons which carry more exotic exchange statistics. One property of these anyons is a degenerate groundstate. While the exchange bosons, fermions and abelian anyons only lead to a phase shift of the global wave function, the exchange of two non-abelian anyons can perform a unitary transformation from one degenerate ground state to another, changing the wave function non-trivially.

$$\text{Abelian Anyons: } |\Phi(x, y)\rangle \Rightarrow e^{i\phi/2} |\Phi(y, x)\rangle \quad (4)$$

---


$$\text{Non-abelian Anyons: } |\Phi(x, y)\rangle \Rightarrow e^{i\frac{\phi}{2}U} |\Phi(y, x)\rangle \quad (5)$$

The separation of this degenerate ground state from other states is sufficient to define topological order and makes it useful for quantum computation. It creates a protected Hilbert-space which is insensitive to perturbations of the system, similar to a given symmetry in a system. Another way of viewing the topological protection is that the information is stored globally and is not located at a specific point like e.g. the spin of an electron, which makes it immune to local perturbations. Single anyons can be described by their *lifeline*, which describes their position in space and time (see Figure 2.2) [18]. Exchanging these particles *braids* their lifelines and transforms the system into another ground state, where topologically equivalent exchanges lead to the same ground state [19]. Imagining a whole plane of these particles, exchanging particles on this lattice is equivalent to performing non-commuting unitary operations. To read out the state of a system in the end these anyons can be fused at the end of your operation. This braiding operation is yet to be successfully performed, proposed system which should host these topological excitations are the 5/2 state of the fractional quantum hall effect [20, 21], edge modes of a topological insulator [22] and the Majorana zero modes we are aiming at in this work.

### 3 Topology in Condensed Matter

The quest for excitations with exotic exchange statistics in condensed matter systems has been going on for the last 30 years. We briefly introduce fundamental concepts in this chapter, spend some time on Andreev bound states as they are predicted to mimic predicted signatures of topological phase transitions and then talk about the fundamentals of this phase transition.

#### 3.1 Superconductivity

Discovered in 1911 by Dutch physicist Heike Carmerling Onnes [23], superconductivity describes the effect where a material cooled below a certain material specific critical temperature  $T_C$  suddenly loses all electrical resistance (perfect conductance) and simultaneously expels all magnetic field lines (perfect diamagnetism), the so called Meissner effect. The perfect diamagnetism is not just a consequence of perfect conductance - a classical perfect conductor would trap flux lines inside itself instead of expelling them. As one of the first discovered purely quantum mechanical effects, it's first full description in 1957 by John Bardeen, Leon Neil Cooper and John Robert Schrieffer (known as BCS-Theory) [24] is based on the idea of the formation of bosonic excitations which consist of two electrons each paired with opposite momentum and spin ( $k \downarrow$  and  $-k \uparrow$ ) - the Cooper pair (CP). These Cooper pairs form in the low temperature regime, where the attractive force between electrons due to lattice phonons becomes comparable to thermal excitations  $k_B T$ . Suddenly not governed by the Pauli exclusion principle anymore, all electron can condense into the lowest energy state<sup>2</sup>.

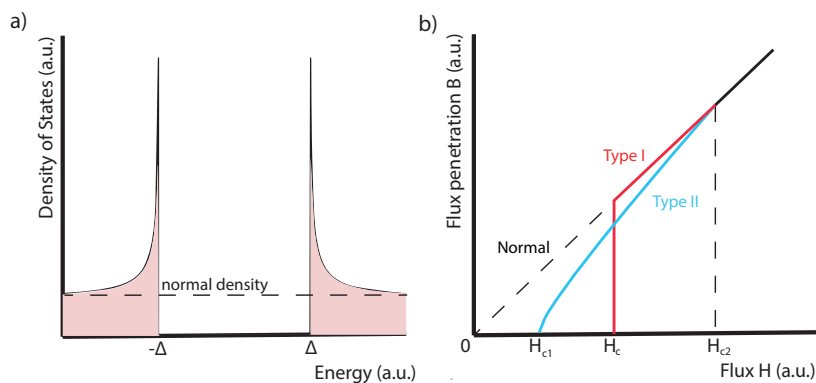


Figure 3.1: a) Superconducting density of states with the coherent peaks at the border of the superconducting gap. Dashed line represents the density of states of a normal metal. b) Flux penetration in dependence of total flux of a type I (red), type II (blue) superconductor and a normal metal (adapted from [26])

The formation of a CP saves an energy  $\Delta$ , so electrons around the Fermi surface  $E_F \pm \Delta$  condense into CPs which leads to the formation of a characteristic energy gap (Figure 3.1a) for which the density of states is given by  $E/\sqrt{E^2 - \Delta^2}$  at  $T = 0$ . The condensed states

<sup>2</sup>Here is to be mentioned that the Pauli-exclusion principle is still present, it's the mechanism which differentiates superconductivity from its phenomenological brother - the Bose-Einstein condensate. It prevents the Cooper pairs from occupying the same momentum state and prevents the complete mapping of this problem onto the Bose-Einstein condensate. [25]

accumulate at the borders of an energy gap forming the so called *coherence peaks*, where they can be populated by spending  $2\Delta$  to break apart a CP.

To see the nature of the quasiparticle excitations in this system we start of with an s-wave pairing Hamiltonian

$$\mathcal{H} = \sum_{k\sigma} \epsilon_k n_{k\sigma} + \sum_{kl} V_{kl} c_{k\uparrow}^\dagger c_{-k\downarrow}^\dagger c_{-l\downarrow} c_{l\uparrow} \quad (6)$$

where the first sum acts over all momenta  $k$  and spin configurations  $\sigma \in \{\uparrow, \downarrow\}$ , with the number operator  $n_{k\sigma} = c_{k\sigma}^\dagger c_{k\sigma}$ , the energy associated with each fermion  $\epsilon_k$  and the strength of the scattering potential to scatter a pair of electrons from a state with momenta  $(k', -k')$  to  $(k, -k)$ . On a side note this Hamiltonian does only contain terms paired up as  $(k \uparrow, -k \downarrow)$ , because unpaired terms do not appear in the BCS ground-state wave function. To diagonalize this Hamiltonian a linear transformation to a new set of Fermi operators is introduced.

$$\begin{aligned} c_{k\uparrow} &= u_k^* b_{k,1} + v_k b_{k,2}^\dagger \\ c_{k\downarrow}^\dagger &= -v_k^* b_{k,1} + u_k b_{k,2}^\dagger \end{aligned} \quad (7)$$

and

$$b_{k,1} = t_k c_{k\uparrow} + s_k c_{k\downarrow}^\dagger \quad (8)$$

with the new coefficients  $u_k$  and  $v_k$ ,  $t_k$  and  $s_k$ . These excitations  $b_{k,i}$ , so called *Bogoliubons* consisting of an electron and a hole part, not necessarily with equal contributions, turn out to describe the elementary excitations of the system. The full description of the BCS theory is beyond the scope of this thesis, for the interested reader I highly recommend Tinkham for further details [26].

Superconductivity can be destroyed by applying a critical external field  $H_C$ , extending the temperature over the critical temperature  $T_C$  or by a critical current  $I_C$  running through the superconductor. One has to distinguish two types of superconductors here. Type I superconductors completely collapse upon reaching its critical field  $H_C$  (Figure 3.1b blue) while type II superconductors start to allow for pinned flux lines above a critical field  $H_{C1}$  increasing in size upon completely destroying superconductivity at  $H_{C2}$  (Figure 3.1b red).

### 3.2 Andreev reflection

Andreev reflection describes the scattering process of an incident electron at a normal-superconductor interface. In addition to the specular reflection, where a spin up electron with momentum  $k$  and Energy  $+E$  is reflected as a spin up electron with opposite momentum  $-k$  not contributing to current, another process is possible. Alexander F. Andreev [27] and Saint James [28, 29] realized that a hole with opposite spin and opposite momentum can be reflected instead. As long as the energy of the incident electron is smaller the energy gap  $E < \Delta$ , there are no available states for the electron to continue its path. Mathematically the electron has to obey the pairing  $c_{k\uparrow}^\dagger c_{-k\downarrow}^\dagger$ . To occupy a state in the superconductor, it pairs up with another electron with energy  $-E$ , opposite spin  $\downarrow$  and opposite momentum  $-k$  from the Fermi sea of the normal conductor to form a Cooper pair. This leaves behind a hole with spin  $\downarrow$  and momentum  $-k$ , traveling in the opposite direction. This leads to a

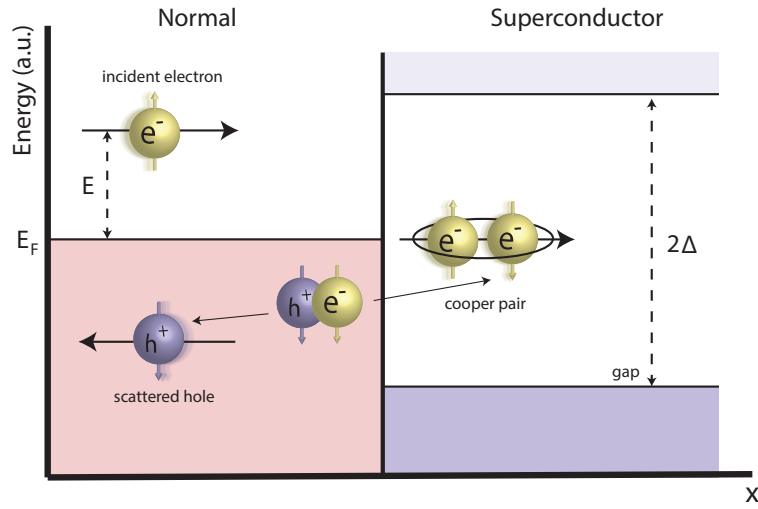


Figure 3.2: Schematic of an Andreev reflection. An incident electron with energy  $+E$  and momentum  $k$  gets scattered at the normal-superconductor boundary as a hole with energy  $-E$  and momentum  $-k$  and to form a Cooper pair in the superconductor.

doubling of conductance for energies below  $\Delta$ .

The wave function of this state obtained by the Bogoliubov-de Gennes formalism has a complex wavevector. This leads to an evanescent wavefunction inside the superconductor which decays at  $E = 0$  on the length scale of the superconducting coherence length

$$\xi = \frac{2\mu}{\Delta k_F} = \frac{\hbar v_F}{\Delta} \quad (9)$$

with the chemical potential  $\mu$ , the Fermi wave vector  $k_F$  and the Fermi velocity  $v_F$ . The wavefunction of the nongapped system extending into the superconductor leads to a decrease of  $T_C$ . On the other side, the wavefunction of the gapped system penetrates the normal conductor and gives rise to the so called proximity effect.

### 3.3 Superconducting proximity effect

At the boundary of a normal-superconductor system, properties of both materials 'leak' into the other. On one side unpaired electrons of the normal conductor leak into the gapped superconducting system leading to a decrease in the critical temperature  $T_C$ , weakening the gap. On the other side Cooper pairs cross the boundary and open up a gap in the previously ungapped system, proximitizing the semiconductor. This arises from the abruptness of the transition between the two materials, electrons and cooper pairs traversing between these boundaries can not follow immediately after entering the new system. Cooper pairing is destroyed over scattering events determined by the characteristic length scale - the coherence length of the semiconductor. Experimentally it was first observed in 1996 [30].

### 3.4 Andreev bound states

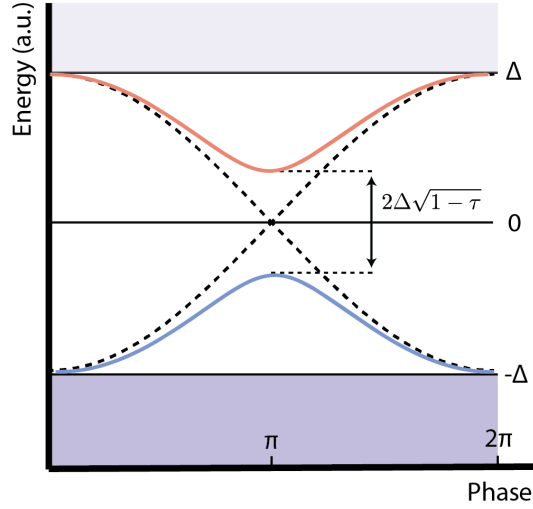


Figure 3.3: Energy spectrum of an Andreev bound state in dependence of the superconducting phase difference  $\delta$ . The blue and red line correspond to  $\tau = 0.9$ . Dashed line represents the case with no specular reflection  $\tau = 1$ . Adapted from [31]

Andreev bound states (ABS) are fermionic states bound by Andreev reflection inside a superconductor - coherent normal conductor-superconductor (S-N-S) structure with a phase difference of  $\delta$  between the two superconductors. Electrons are reflected at the two normal-super interfaces through Andreev reflection multiple times, creating standing waves. These are addressable as energy states in the superconducting energy gap [32]. For a thin normal conducting region, the layer essentially acts as a scattering impurity. For the condition of the length of the coherent conductor  $l$  being shorter than the superconducting coherence length  $\xi$ , a pair of ABS lives inside the superconducting gap at energies  $\pm E_A$  localized at this scattering impurity [31].

$$E_A = \pm \Delta \sqrt{1 - \tau \sin^2 \left( \frac{\delta}{2} \right)} \quad (10)$$

where the  $\tau$  represents transmission rate across this scattering impurity

$$\tau^{-1} = 1 + \left( \frac{\eta}{k_F} \right)^2 \quad (11)$$

with  $\eta = \frac{mV}{\hbar^2}$  being the inverse of the scattering length.  $V$  in this case is the height of the scattering potential, modeled as a delta function. This is depicted in Figure 3.3 as the blue and red lines for the positive and negative solution. The energy of these states is highly dependent on the phase difference  $\delta$  across the impurity. For a phase difference of 0 and  $2\pi$  these ABS disappear into the continuum of states. Even for the ballistic case  $\tau = 1$  ABS exist and their energies reduce to (Figure 3.3 dashed line)

$$E_A = \pm \Delta \cos \left( \frac{\delta}{2} \right) \quad (12)$$

Turning on the scattering potential leads to additional specular reflexion. This opens up

a gap at  $\delta = \pi$  of  $E = 2\Delta\sqrt{1-\tau}$ .

As they are localized at the scattering impurity, the wave function of the ABS decays on a characteristic length scale [31]:

$$K_A^{-1} = \frac{\xi}{\sqrt{1 - \left(\frac{E_A}{\Delta}\right)^2}} = \frac{\xi}{\sqrt{\tau} \left| \sin\left(\frac{\delta}{2}\right) \right|} \quad (13)$$

### 3.4.1 Andreev bound states with charging energy

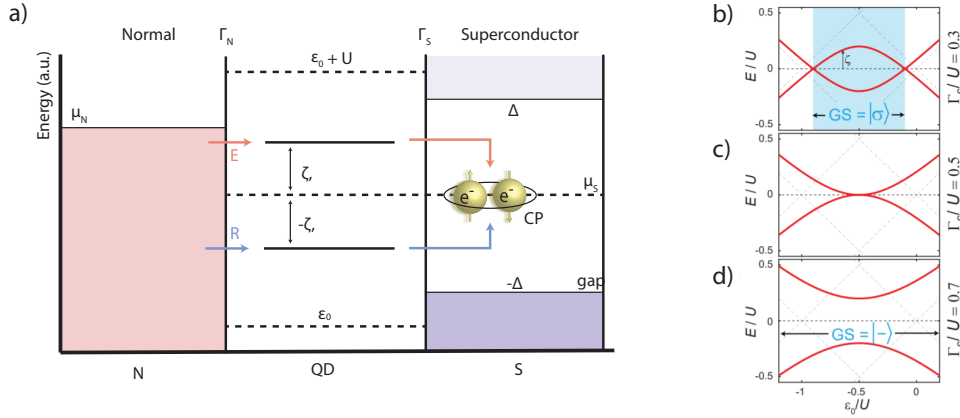


Figure 3.4: a) Schematic of a normal-quantum dot-superconductor interface. Adapted from [33] b) Andreev bound state in the charging energy dominated regime [34] c) Andreev bound state at the transition between charging energy and superconducting pairing dominated regime [34] d) Andreev bound state in the superconducting pairing dominated regime [34]

So far we considered the phase dependence of a point-like impurity, now we consider a quantum dot like impurity. The term ABS evolved to represent a class of subgap states. Another way of realizing these states is a single degenerate mode quantum dot strongly coupled to a superconductor with the coupling  $\Gamma_S$ . The superconductor exchanges Cooper pairs with the even parity states of the quantum dot resulting in new eigenstates of the hybrid system. In the superconducting atomic limit ( $\Delta \Rightarrow \infty$ ) the emerging singlet eigenstate can be written as a superposition of the empty and doubly occupied quantum dot [34]

$$|-\rangle = u |0\rangle - v^* |\uparrow\downarrow\rangle \quad (14)$$

with the Bogoliubov de Gennes amplitude  $u$  and  $v$  and the corresponding eigenenergy  $E_-$ . The orthogonal eigenstate reads the following:

$$|+\rangle = u |0\rangle + v |\uparrow\downarrow\rangle \quad (15)$$

with eigenenergy  $E_+$ . The odd charge states stay unperturbed doublets:

$$|\sigma\rangle, \sigma \in \{\uparrow, \downarrow\} \quad (16)$$

In this system two energy scales determine the behavior of the system[35]: The charging energy of the quantum dot  $U$  coupled to a normal conducting lead and the coupling to the superconductor  $\Gamma_S$ . These eigenstates can be probed by electron tunneling spectroscopy. Depending on the variables  $\Delta$ , the charging energy  $U$ , the energy level of the QD relative to the Fermi level  $\epsilon_0$  and  $\Gamma_S$  either the doublet or the singlet is the ground state of the system while the other represents the excited states.

The following example assumes  $|\sigma\rangle$  as the ground state of the system. When the chemical potential  $\mu_N$  matches the Andreev addition energy  $\zeta = |E_- - E_\sigma|$ , transport through the ABS is possible. As depicted in Figure 3.4, charge is carried by an electron tunneling from N into the QD and transferring the system from the ground state  $|\sigma\rangle$  to the excited state  $|- \rangle$  (E). A relaxation process (R) is possible when a second electron tunnels into the  $-\zeta$  part of the ABS which transfers two electrons as a CP pair into the superconductor. This second electron leaves behind a hole in the normal lead which is the Andreev reflected hole discussed in the previous chapter.

The characteristic bias and gate dependence of ABS forms *loops* (see Figure 3.6b,c,d). These represent the competition between the charging energy  $U$  and the strength of the coupling to the superconductor  $\Gamma_S$  responsible for the superconducting pairing on the QD. For a system that is dominated by the charging energy  $U$ , the doublet with odd electron pairing is energetically preferred and one finds a gate induced transition where the system changes from one ground state to the other (Figure 3.4b). The loops intersect in this case at the point of  $\zeta = 0$ . For a system that is dominated by the superconducting pairing, even parity is preferred and the singlet stays ground state - no gate induced transition can be found (Figure 3.4d). The transition between the two happens at  $\Gamma_S/U = 0.5$  and is depicted in Figure 3.4c). A more thorough theoretical description of these crossovers can be found in Meng *et al.*[36].

### 3.4.2 ABS in a three terminal measurement

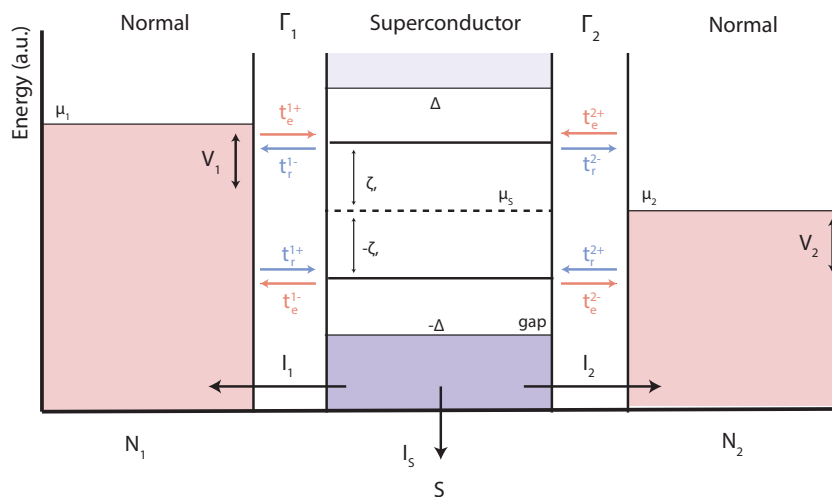


Figure 3.5: Extended model from Figure 3.4a, two normal leads and a superconducting lead coupled to a quantum dot. Tunneling processes to the electron/hole part of the ABS are represented by blue and red arrows. Adapted from [34]

At this point a simple model to describe a three terminal measurement of Andreev bound states with two normal leads  $N_1$  and  $N_2$  and one superconducting lead  $S$ .) is introduced. We follow a model[34] which extends the model discussed in chapter 3.4.1. It considers a quantum dot with a single degenerate mode coupled to two normal leads  $N_1$  and  $N_2$  by the couplings  $\Gamma_1$  and  $\Gamma_2$  and to a superconducting lead  $N_S$  via the coupling  $\Gamma_S$ . It operates in the limit of  $\Delta \Rightarrow \infty$ . For  $E < \Delta$  only transport through the ABS has to be considered. In this model, bias is applied at  $N_1$  which sweeps the chemical potential  $\mu_1$ . The other two chemical potentials are held at zero  $\mu_1 = \mu_2 = 0$ . In our experiment we sweep bias on  $N_1$  and  $N_2$  separately while leaving the other fixed at zero with a grounded SC lead, so this assumption is sensible. Again our system possesses the GS-ES properties from the two terminal model discussed earlier. In this case we assume the singlet  $|-\rangle$  to be the GS of our system, but the model produces the similar findings in nonlocal conductance with the two states swapped. The state occupation probabilities of our system are labeled  $P_{GS}$  and  $P_{ES} = 1 - P_{GS}$ . In the steady state approximation one receives:

$$\frac{d}{dt}P_{ES} = t_e P_{GS} + t_r P_{ES} = 0 \quad (17)$$

This gives us  $P_{GS} = \frac{t_r}{t_e + t_r}$  and  $P_{ES} = \frac{t_e}{t_e + t_r}$ . The tunneling rates  $t_r(t_e)$  consist of four processes each which relax (excite) the ABS. The single tunneling rates are depicted in Figure 3.5 as red and blue arrows, where blue arrows correspond to an event associated with a relaxation processes of the ABS and red to excitation processes from GS to ES. Their superscript  $+$  ( $-$ ) indicates if they add (remove) an electron from the left (1) or right (2) lead to the S-QD system. These rates can be calculated by Fermi's golden rule e.g.:

$$|\sigma\rangle \xrightarrow[1]{+1e} |-\rangle : t_r^{1+} = \Gamma_1 \underbrace{|\langle - | d_{\bar{\sigma}}^\dagger | \sigma \rangle|}_{v^2} f_1(\xi) \quad (18)$$

with the Fermi distribution  $f_{1(2)}(\xi)$  on the left (right) normal lead, the creation (annihilation) operator  $d_{\sigma}^\dagger$  ( $d_{\sigma}$ ) for an electron on the QD with spin (opposite spin)  $\sigma$  ( $\bar{\sigma}$ ) and the previously mentioned BdG amplitudes  $u$  and  $v$  of the ABS.

Subsequently the currents running to or from the leads  $I_1$ ,  $I_2$  and  $I_S = -(I_1 + I_2)$  can be derived and derivated to obtain the differential conductances. The results for  $dI_x/dV_1$  are plotted in Figure 3.6a,b,c for  $\Gamma_1=0.1$  meV,  $U = 3$  meV,  $\Gamma_1 = \Gamma_2$ ,  $V_2 = V_S = 0$  and a finite  $T = 0.5K$  to induce some thermal broadening.

$dI_1/dV_1$  and  $dI_S/dV_1$  show the ABS energy relation depicted in Figure 3.3 pushed through zero energy by the charging energy of the quantum dot. The nonlocal conductance  $dI_2/dV_1$  follows the same trajectory but exhibits a sign change at the degeneracy point. This sign change comes from the direct competition of tunneling rates  $t_r^{1+}$  and  $t_r^{2+}$ : the nonlocal current  $I_2$  is directly proportional to the de Gennes amplitudes  $I_2 \propto u^2 - v^2$ . The crossover point where sign changes from positive to negative differential conductance marks the point where  $u^2 = v^2$ . In this picture, the loops represent the gradual charging of the ABS.

Changing to a more coherent picture, one can identify two different processes happening in this system. The *resonant ABS tunneling* where one electron tunnels from  $N_1$  to  $N_2$  over the ABS (red in Figure 3.6d). The other process is a nonlocal formation of a CP consisting of one electron from both leads often referred as *inverse CP splitting* (blue in Figure

3.6). Both nonlocal processes involve all three leads. Their amplitude is proportional to two individual tunneling rates  $t_{iCPS} \propto t_e^{1+} t_r^{2+}$  and  $t_{rABS} \propto t_e^{1+} t_r^{2-}$ .

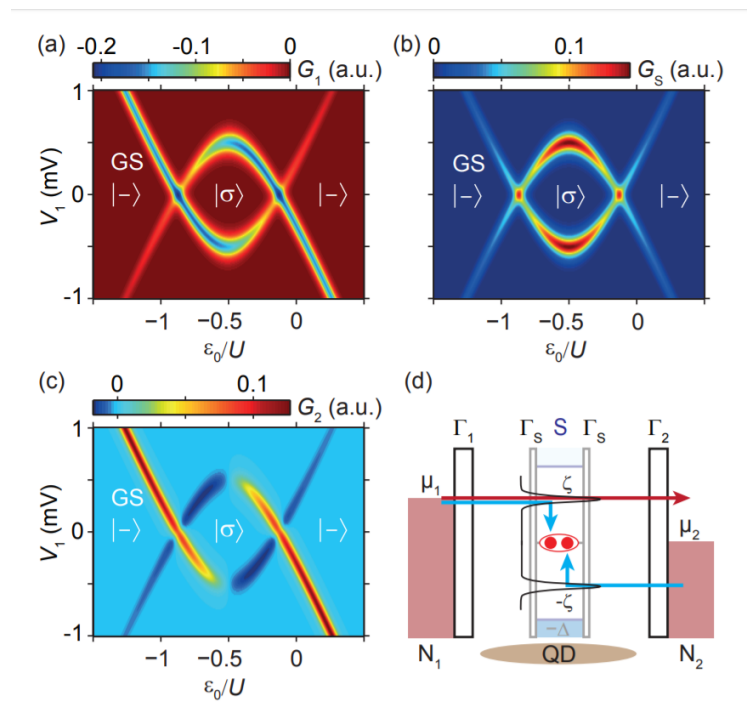


Figure 3.6: a) Expected local conductance on  $dI_1/dV_1$  in this model b) Expected local conductance  $dI_s/dV_1$  of the aluminum lead c) Expected nonlocal conductance  $dI_2/dV_1$  with the sign change at the degeneracy point observed in our experiment d) The two processes that drive the sign change of the nonlocal conductance: resonant ABS tunneling (red) and nonlocal formation of a CP (blue) [34]

### 3.5 1D Kitaev Chain

In 2001 Russian physicist Alexei Kitaev proposed a system in which Majorana zero modes (MZM) form at the boundary [37]. It considers a one dimensional electron tight binding chain with  $N$  sites with p-wave superconducting pairing. Our creation/annihilation operators  $c_i^\dagger, c_i$  refer now to specific sites of the chain  $i$ . In a p-wave paired superconductor adjacent fermionic sites are populated by opposite spins which allows us to omit spin from our Hamiltonian:

$$\mathcal{H} = \sum_i^N \left[ -\mu c_i^\dagger c_i - \underbrace{t (c_i^\dagger c_{i+1} + c_{i+1}^\dagger c_i)}_{\text{Fermion Hopping}} + \underbrace{\Delta c_i c_{i+1} + \Delta^* c_i^\dagger c_{i+1}^\dagger}_{\text{CP Creation/Annihilation}} \right] \quad (19)$$

with the chemical potential  $\mu$ , the hopping amplitude  $t$  and the superconducting energy gap  $\Delta = |\Delta|e^{i\Phi/2}$ . This Hamiltonian contains three major terms. The first one corresponds to the energy related to the number of fermions in the system. The second part is responsible for site hopping, note that every term destroys a fermion on one site and creates it at an adjacent one. The last term corresponds to the creation and annihilation of Cooper pairs. Now we split the real and the imaginary part of our fermion operators into two Majorana operators. In second quantization this reads:

$$c_i = \frac{1}{2}(\gamma_{i,1} + \gamma_{i,2}) \quad \text{and} \quad c_i^\dagger = \frac{1}{2}(\gamma_{i,1}^\dagger + \gamma_{i,2}^\dagger) \quad (20)$$

and subsequently

$$\gamma_{i,1} = c_i^\dagger + c_i \quad \text{and} \quad \gamma_{i,2} = i(c_i^\dagger - c_i) \quad (21)$$

At first, this is allowed and has no immediate physical consequences. Their form is similar to the Bogoliubov quasi particles introduced to explain superconductivity, but they have an additional property of being hermitian  $\gamma_{i,a} = \gamma_{i,a}^\dagger$ , having equal contributions from the electron and hole part and that creating or destroying two Majorana fermions leads back to the original wave function  $(\gamma_{i,a})^2 = (\gamma_{i,a}^\dagger)^2 = 1$ . Replacing our fermion operators in our Hamiltonian gives back:

$$\mathcal{H} = \frac{i}{2} \sum_i^N \left[ -\mu \gamma_{i,1} \gamma_{i,2} + (t + |\Delta|) \gamma_{i,2} \gamma_{i+1,1} + (-t + |\Delta|) \gamma_{i,1} \gamma_{i+1,2} \right] \quad (22)$$

The superconducting phase  $e^{i\Phi/2}$  is hereby included in the majorana operators for simplicity. Now two cases strike the eye. Case I:  $\mu < 0$  and  $\Delta, t = 0$ . Case II:  $\mu = 0$  and  $|\Delta| = t$

$$\mathcal{H} = \frac{i}{2} \sum_i^N \left[ \underbrace{-\mu \gamma_{i,1} \gamma_{i,2}}_{=0 \text{ in case II}} + \underbrace{(t + |\Delta|) \gamma_{i,2} \gamma_{i+1,1}}_{=0 \text{ in case I}} + \underbrace{(-t + |\Delta|) \gamma_{i,1} \gamma_{i+1,2}}_{=0 \text{ in case I and II}} \right] \quad (23)$$

The first case leads to a trivial solution of the Hamiltonian

$$\mathcal{H}_{\text{Triv}} = \frac{i}{2} \sum_i^N -\mu \gamma_{i,1} \gamma_{i,2} = \mu \sum_i^N c_i^\dagger c_i \quad (24)$$

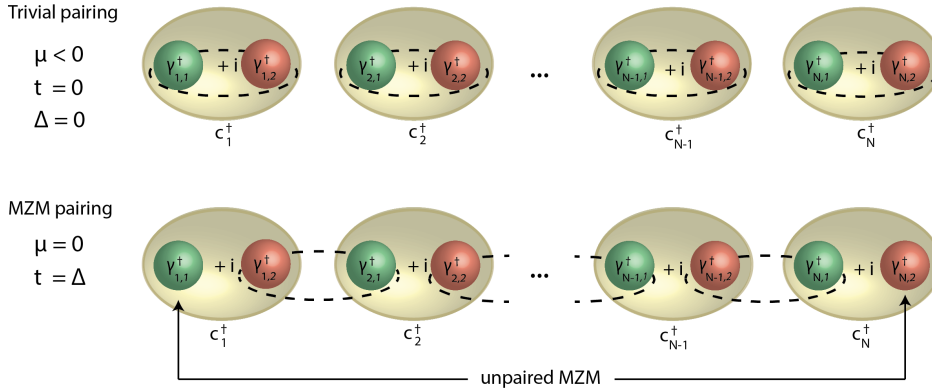


Figure 3.7: Top row: Pairing in the trivial case - Majorana operators at the same sites are paired up, no unpaired MZMS. Bottom row: Pairing in the non-trivial case - Majorana operators at adjacent sites pair up which leaves two unpaired MZMs at the two ends of the wire.

In this case, the Majorana fermion operators are paired up at their respective sites, a gapped phase with no MZMs present. The second case leads to a different phase.

$$\mathcal{H}_{\text{MZM}} = it \sum_i^N -\mu \gamma_{i,2} \gamma_{i+1,1} \quad (25)$$

In this case, Majorana fermion operators are paired up at adjacent sites. But here the  $\gamma_{1,1}$  and  $\gamma_{N,2}$  operators are missing from the Hamiltonian. These are unpaired Majorana fermion operators at living at both ends of the chain which require zero energy for occupancy while all other states require  $\pm t$  energy for occupancy. This means there are zero energy states at the system borders with a gapped bulk. These states can be combined into a highly nonlocal new fermionic state.

$$c_M = (\gamma_{N,2} + i\gamma_{1,1})/2 \quad (26)$$

The ground state is therefore two-fold degenerate as  $c_M^2 = (c_M^\dagger)^2 = 1$  and is best described by its *parity*. One ground state contains an even number of excitations, the other contains an odd number.

To move these two states from zero energy individually is not possible because of particle hole symmetry, this is the previously mentioned topological protection. Them being pinned to zero energy prevents qubits from natural dephasing from energy differences in the time evolution of Schrödinger's equation. The only way to move them from zero energy is to couple the two unpaired modes. This is prevented by their spacial separation and the energy gap in the bulk. To split the Majorana states from zero energy requires to close the gapped bulk in between them at  $|\mu| = -2t$ .

Unfortunately there are no known natural occurring superconductors with p-wave pairing. Fortunately the occurrence of Majorana fermions at the borders of this system is a *topological invariant* so every system with the same topological properties as the p-wave superconductor will give rise to these excitations at their borders. The task now becomes to engineer this new system.

### 3.6 Engineering Majorana fermions in nanowires

Following theoretical proposals [38, 17] one can construct a system with materials currently available today which is described by a Hamiltonian topologically equivalent to a p-wave superconductor. The main four ingredients to form this system are:

1. 1D conductance channel
2. Strong Rashba spin-orbit coupling
3. S-wave pairing superconductivity
4. B-field in direction along the axis of the 1D system

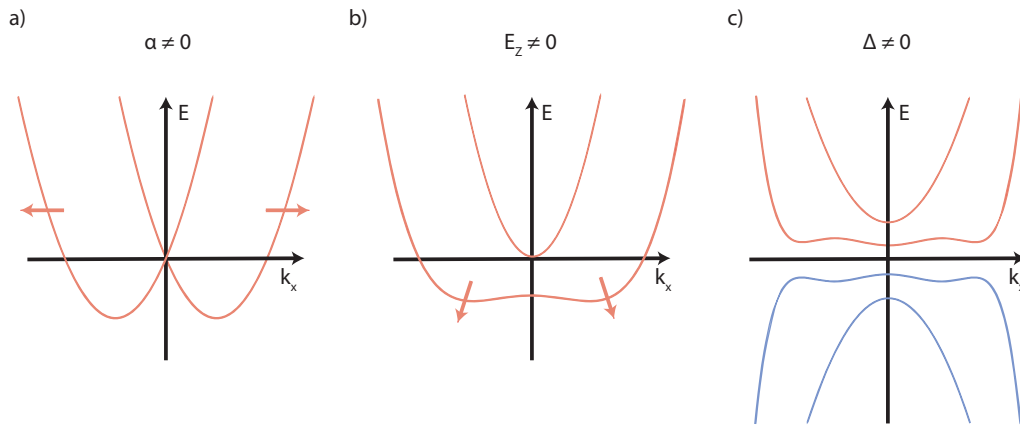


Figure 3.8: a) Spin bands shifted in momentum space by Rashba spin-orbit coupling, magnetic field and superconducting gap still turned off. b) Adding a perpendicular magnetic field breaks time reversal symmetry and turns the crossing at zero momentum into an anti-crossing. c) Proximity-induced superconductivity enforces particle-hole symmetry and opens up a gap bulk with topological excitations at the border of the system. [13]

The Hamiltonian to describe this system can be written as

$$\mathcal{H} = \left[ \frac{k_x^2}{2m} - \mu \right] \tau_y + \alpha k_x \sigma_y \tau_y + E_z \sigma_z + \Delta \tau_z \quad (27)$$

with the Pauli-matrices  $\sigma_i$  and  $\tau_i$ . At the beginning we start by only considering the kinetic energy term and then subsequently turning on spin orbit coupling  $\alpha \neq 0$ , the magnetic field  $B = 0$  and superconductivity  $\Delta = 0$ . The parabolic energy dispersion  $\frac{k_x^2}{2m}$  with spin-degeneracy (not depicted) describes our one dimensional conductance channel placed along the x-axis of our system. Turning on Rashba spin orbit coupling  $\alpha \neq 0$  (Figure 3.8a) splits this level into two sub-bands shifted in energy by their spin interaction with the Rashba-field. As the Rashba-spin orbit is the cross-product of electric field and momentum, we choose it to be along the y-axis without loss of generality. Turning on the parallel magnetic field  $B \neq 0$ , which we assume to be along the z-direction, leads to a finite Zeeman energy  $E_Z = g\mu_B B$  with the Bohr magneton  $\mu_B$  and the semiconductor g-factor  $g$

and breaks time reversal symmetry. This turns the previous crossing at zero momentum into an anti-crossing leading to two separate spin bands (Figure 3.8b). Placing the chemical potential  $\mu$  inside the gap this anti-crossing allows only one (yet still momentum dependent) spin direction and with it the ability to induce spin-less superconductivity. Now finally turning on superconductivity (Figure 3.8c) with finite  $\Delta$ , one opens up a gap between the solutions of the Bogoliubov-de Gennes equation associated with electron (red) and holes (blue). Note that the amount of band doubles due to particle-hole symmetry. For small  $\Delta$  this is the topological regime with a gapped bulk of the wire which forms MZM at the edges of the system. For increasing  $\Delta$ , one finds the gap closing at  $|B| = \sqrt{\Delta^2 + \mu^2}$  and reopening in a non-topological regime. The condition for the topological regime is therefore:

$$|B| > \sqrt{\Delta^2 + \mu^2} \quad (28)$$

The transition into the topological regime and the measurement of the zero bias conductance peak has sparked theoretical discussion whether or not this signature can only be caused by MZM modes forming at the ends of the nanowire. Kells *et al.* [39] and Liu *et al.*[40] found that trivial ABS states can cause a indistinguishable signature in tunneling spectroscopy in the trivial regime. This hinders the experimental verification of the topological transition solely through one sided local tunneling spectroscopy and different methods are necessary to distinguish trivial ABS from MZMs.

## 4 A new platform for topological quantum computation

Now that we covered the theoretical foundation of our approach it is time to show the experimental successes on the road to non-abelian excitations and then to introduce selective area grown nanowires and nanowire networks.

### 4.1 Signs of Majorana bound states in nanowires

The first predicted signs of Majorana bound states were found in 2012 by the Kouwenhoven group in Delft in an epitaxially grown InSb wire, proximitized by one superconducting lead and one tunneling barrier to probe the density of states of the hybrid structure over tunnel spectroscopy (see Figure 4.1). They observed a zero bias peak (ZBP) at finite field, which was stable over a range of field and electron density values [41]. This is caused by a state at zero energy at the end of the wire. After this, other groups observed these ZBPs as well in InAs nanowires with epitaxial aluminum [42] and in two-dimensional electron gases (2DEG) [43]. But looking at the final goal for a moment, a universal quantum computer with  $10^3$  to  $10^6$  qubits, these solutions of probing the existence of Majorana zero modes lack scalability to be used in future topological quantum computing architectures. One possible qubit structure is presented in Figure 4.1 which has topological islands hybridizing over coupled quantum dots. At the highlight regions topological regions couple and calculations and readout are performed by the hybridization of MZMs. All of these architectures require a continuous topological phase forming in the system. As these nanowire networks are not possible to be constructed out of single nanowires a different platform is necessary to achieve these architectures in the future.

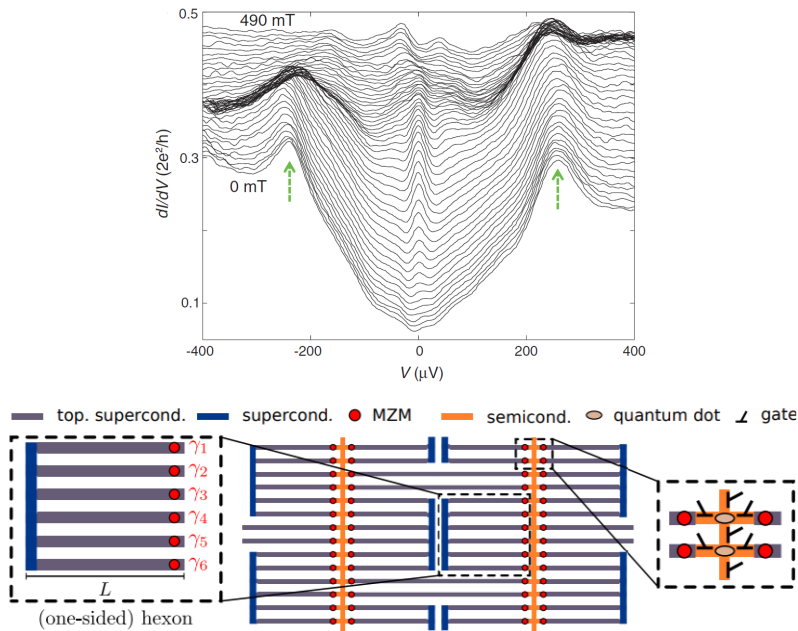


Figure 4.1: Top: Waterfalldiagram of the first observed zero bias peak in [41]. Bottom: A proposed topological qubit architecture using a nanowire network [44]

## 4.2 Selective area growth

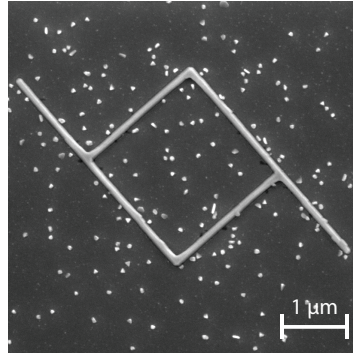


Figure 4.2: An MBE selective area grown nanowire network with good structural integrity and lacking selectivity.

Measured nanowires so far have been grown by the vapour-liquid-solid (VLS) method. It uses gold particles as catalyst for one dimensional epitaxial<sup>3</sup> growth [45]. This leads to good epitaxial match and structural integrity but lacks scalability. Growing semiconductor structures in predefined shapes with high purity and structural integrity is an essential tool to realize the proposed architectures presented in the previous chapter. To achieve this, a III-V wafer (in our case either InP or GaAs) is capped with a layer of oxide (SiO). The substrate is chosen to be a semi-insulator at base temperature (20 mK) to electrically isolate the to be grown structures. Then using a wet or dry etch, trenches of oxide are removed to expose the bare semiconductor (see Chapter 5.2). Now one can grow the chosen semiconductor (InAs) in these trenches by either molecular beam epitaxy (MBE) or chemical beam epitaxy (CBE). MBE is taking place in a ultra high vacuum (typically  $10^{-8}$  to  $10^{-12}$ ), where crucibles enclosing selected elements (in this case indium, gallium, arsenic, phosphorous) are heated in order for the elements to sublime or evaporate. After, the materials are introduced into the growth chamber in form of vapor phase directional fluxes targeted at the substrate, which initiates the epitaxial crystal growth. Deposition rates are controlled by specific growth parameters like substrate temperature, material fluxes and material flux stoichiometry. These parameters have to be optimized for the *structural integrity* of the semiconductor and the *selectivity* of the growth. Selectivity meaning that the semiconductor only grows in the predefined trenches and not on other parts of the die. In Figure 4.2 a SAG nanowire network with good structural integrity and suboptimal selectivity is depicted. The grains surrounding the network are made of semiconductor that has grown on top of the oxide layer.

In CBE additional chemical carrier precursors are used which lead to a lower necessary vacuum but also to a less pure deposited layer of semiconductor due to carbon impurities. It has a larger growth parameter space [46] for which the growth succeeds, so CBE grown SAG has had a slight edge in quality as of the date of this thesis.

The direct deposition of the final semiconductor (meaning the semiconductor constituting the transport channel) creates an interface with unwished properties between

<sup>3</sup>meaning the growth orients itself at the underlying crystal structure

the lattice mismatched substrate and nanowire. Our measurements have shown that this boundary makes *pinch off*, the change from conductor to insulator of a specific region of the wire through removal of charge carriers, more difficult. This might be related to a 2DEG forming at the boundary or the conduction through impurities.

So a more sophisticated approach is to first grow a buffer layer (e.g. InGaAs) in between to allow for smoother band bending to avoid forming a potential well at the interface and a gradial match of lattice constants [47]. Then in the final stage of this procedure, a superconductor (Al) is deposited at an angle from a specific direction in situ. The angle is roughly  $35^\circ$  to  $45^\circ$ . Only one facet of the wire gets coated with Al so it stays gateable from the other side. Because vacuum is not broken between the growth of the semiconductor and the deposition of the metal no native oxide layer forms in between the two which leads to an optimal interface at the boundary.

In this work I worked on material from three different sources and developed working recipes for each of them.

1. From the group of *Peter Krogstrup* at the University of Copenhagen MBE grown InAs wires with InGaAs buffer on either a GaAs or InP substrate were used.
2. The group of Chris Palmstrøm from *UCLA* provided CBE grown InAs with InAsP buffer on InP substrate.
3. From *Purdue University* and the group around *Mike Manfra* MBE grown InAs on InGaAs buffer on a GaAs substrate was used.

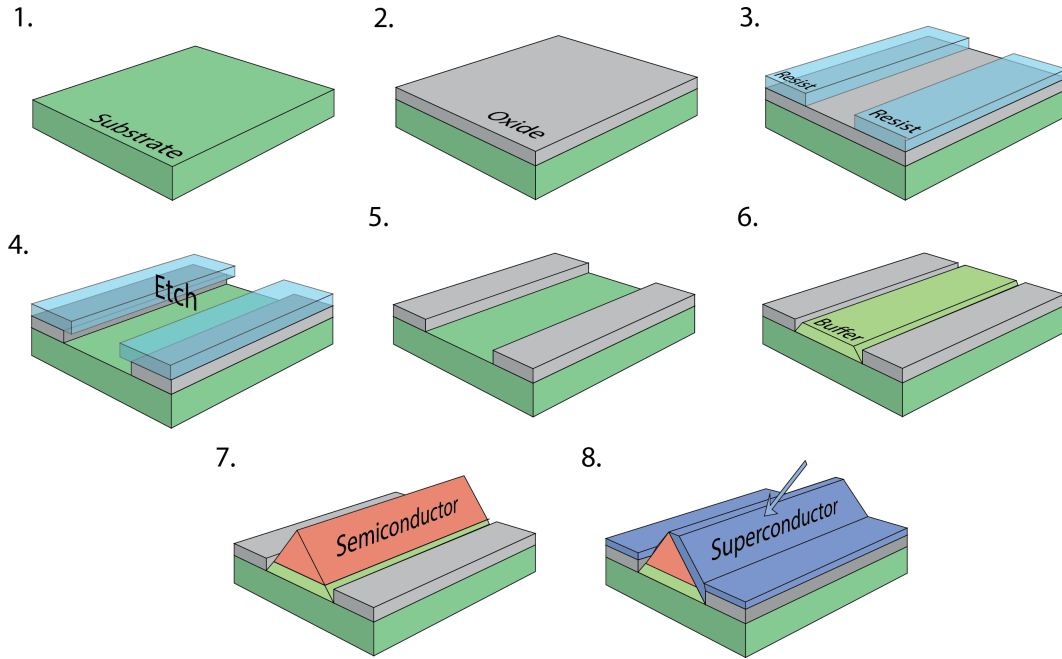


Figure 4.3: Growth process of selective area grown structures in an MBE. First a III-V Substrate (1) is capped with silicon oxide (2) deposited over atomic layer deposition (ALD). A mask with the desired geometries is applied to the wafer (3) via electron beam lithography (see Section 5.2). A selective wet etch removes unwanted oxide but leaves the substrate unharmed (4). After the mask is removed (5), the sample is loaded into a molecular beam epitaxy machine (MBE) and the first layer of semiconductor (Buffer) is grown (6). After this the semiconductor is grown on top (7). Still in situ to avoid a native oxide layer forming, a superconductor is deposited at an angle to cover one facet of the grown structures (8). Figure partly adapted from [47]

## 5 Measurement and Fabrication

### 5.1 Dilution refrigerator

As mentioned before, high temperatures broaden or completely dominate the quantum mechanical effects that one wishes to measure. Therefore the system has to be cooled down to a regime where the energy of thermal photons  $k_B T$  is much lower than the energy scale of the effect one wants to observe. The samples in this thesis are cooled down to 20 mK by a dilution refrigerator *Blue Fors Quick Test BF-XLD1000*, also referred as cryostat, using the properties of a  $^3\text{He}^4\text{He}$  mixture in a two step cooling process. Electron temperatures estimated in SIS-junctions give an electron temperature of roughly 40mK. The cryostat consists of a vacuum chamber for thermal isolation from the environment. Over multiple stages separated by heat switches the plates are gradually cooled down from room temperature to *base temperature*, the lowest achievable temperature in this setup. In the first step all stages and the  $^3\text{He}^4\text{He}$  mixture are cooled down to 4K over a pulse tube cooling system. After reaching 4K, the stages are thermally isolated by deactivating the heat switches. These consist of two copper heat exchanger parts surrounded by a steel tube with low thermal conductance. A pump allows for an exchange gas to be filled or removed from the heat switch which toggles thermal conductance between the stages.

The  $^3\text{He}^4\text{He}$  mixture is then compressed and forced into a flow impedance, condens-

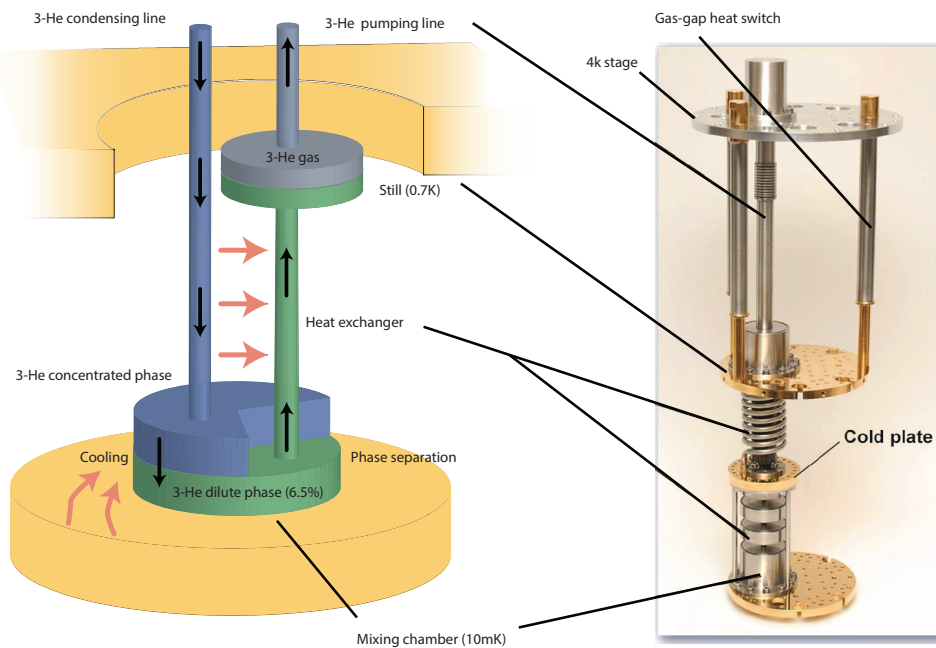


Figure 5.1: Schematic of the dilution unit of a dilution refrigerator. Through compression the  ${}^3\text{He}{}^4\text{He}$  mixture separates into two phases: concentrated  ${}^3\text{He}$  phase (blue) and a  ${}^3\text{He}{}^4\text{He}$  diluted phase (blue) consisting mainly of  ${}^4\text{He}$ . Continuous pumping on the still removes  ${}^3\text{He}$  from the diluted phase and reintroduces it compressed again on the downwards path, forcing it through the phase boundary. This requires energy which gets removed from the coupled lowest stage which is thermally connected to the sample. Adapted from [48]

ing it at the bottom of the fridge into two phases [49]: a helium  ${}^3\text{He}$  concentrated phase (green in Figure 5.1) and a diluted phase consisting mostly of  ${}^4\text{He}$  (blue in Figure 5.1). Pumping on the still mostly removes  ${}^3\text{He}$  because of the two different vapor pressures of the isotopes, which is gathered and compressed back into circulation. At the mixing chamber the compressed  ${}^3\text{He}$  is forced through the phase boundary, a process requiring energy which is taken from the mixing chamber. An osmotic pressure leads  ${}^3\text{He}$  through the diluted phase back to the still closing the circuit. Cooling power is dependent on the flow rate, which can be increased by heating the still to increase vaporization. The lower temperature limit of 20 mK is set by the not totally decoupled environment.

## 5.2 Lithography

Electron beam lithography (EBL) is a standard technique in modern semiconductor technology allowing to create structures with nanometer precision. The process is repeatable so it is possible to build up (in a bottom up approach) or take away (in a top down approach) layer by layer. At the beginning of each step, a liquid drop of *resist* is applied to your die. The resist consists of polymers, in our case of poly methyl methacrylate (PMMA) or methyl methacrylate (MMA). Excess resist is *spinned* away in a centrifuge (*Spinner*) so that a layer of polymer with a uniform height profile stays behind. Then in an EBL system, which is essentially an electron microscope with controlled stage drive and beam shutter,

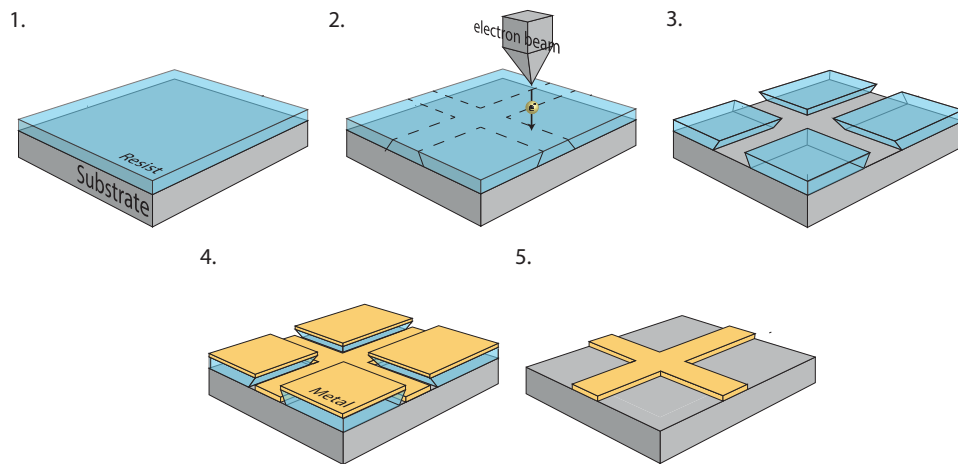


Figure 5.2: 1.) The die is covered with resist 2.) an electron beam exposes a predefined pattern breaking polymer chains of the resist and increasing solubility. 3.) The die is developed and previously exposed patterns get removed while leaving behind a protective layer of resist 4.) In a thin film deposition chamber a metal gets evaporated on the surface, covering the entire die with one layer. 5.) Development in a stronger solvent removes the leftover resist and washes away excess metal only leaving behind the exposed patterns.

a pre-defined pattern is exposed. The high velocity beam breaks up the polymer chains of the exposed regions which increases their solubility. The pattern is designed beforehand in standard 2D CAD programs and corrected for back scattered electrons in specialized software. Even with this correction a small undercut is present at the borders of the resist. The short development in a solvent dissolves the exposed regions, a short rinse in a neutral solvent completes the development. In a thin film deposition chamber, metal is deposited which covers the entire surface, sticking directly to the wafer in previously exposed regions. On the rest of the wafer the resist acts as a protective layer, preventing adhesion to the surface. After metal deposition, *lift-off* in a more potent solvent than before dissolves the remaining polymers and washes away undesired metal films, leaving behind the predefined structures.

### 5.3 Wet etch

A delicate process after growth is the wet etch of the aluminum covering the wafer which warrants its own chapter. The pure metal is covered by a native layer of oxide of 3nm. The etching rates of AlO and Al are roughly 10:1 which allows for the etchant to create an undercut if etching time is not carefully adjusted. Because the procedure involves a liquid, it is more sensitive to small holes and suboptimal surface adhesion of the resist than thin film deposition. After development, small pockets of missing resist (see Figure 5.3) can cause running etchant. To reduce these inhomogeneities, MMA is used as resist instead of PMMA for etching masks. Because of shorter polymer chains the resist has a smaller viscosity and is able to fill small gaps at the wire boundary more efficiently. MMA is highly sensible to dose so the absolute dose window for optimal etching results is much lower than for PMMA (around  $30 \mu\text{C}/\text{cm}^2$  for MMA see Figure 5.3 b). Shorter chains also mean that the difference in solvency between exposed and not exposed MMA is smaller and the developing solvent also attacks the protective resist. So developing time and dose are

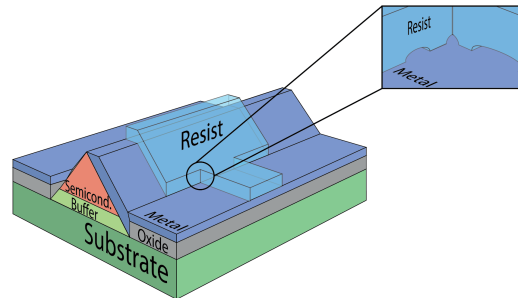


Figure 5.3: Schematic of air pockets forming at the boundary of the wire leading to a lesser quality etch.

two additional factors which need careful adjustment. As a last measure to close existing pockets after development time, one can bake the resist over the reflow temperature of MMA ( $120^{\circ}\text{C}$ ) for a short time to fill possible gaps with reflowing resist.

My work included fabrication on materials from different sources and with different thicknesses of epitaxial Al and AlO. For a fast optimization of etching duration and exposure doses the following scheme has been developed. Patterns of 100nm wide lines separated by increasing distances from 25nm to  $1.3\mu\text{m}$  and test etching windows form the basic test design. This design is exposed at varying doses on outer parts of the SAG wafer covered by aluminum but not containing any SAG structures (to save material if scarce). Each of these chips is then etched for a different duration and investigated under a scanning electron microscope (SEM). Here quality of etch in terms of leftover chunks of aluminum in etching windows and roughness of etching borders becomes apparent. To determine the overetch for each configuration, the last two still clearly separated lines are determined. Their separation distance in the original design is twice the overetch. Points below the lines act as visual aids.

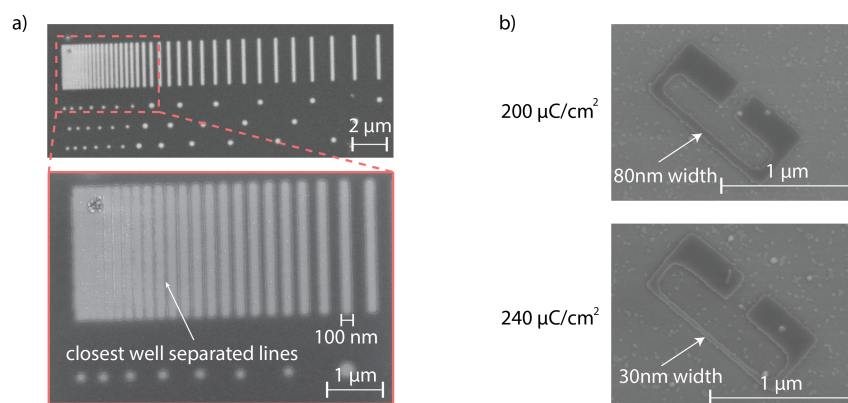


Figure 5.4: a): Pattern for fast determination of the over etch. Dark surface corresponds to the remaining aluminum, bright surface is the bare oxide. b) Difference in precision of etch at different doses with otherwise equal processes. Highlighted line is 140nm in design. Leftover aluminum around the structures hints at a slightly too low etching time.

## 5.4 Device Fabrication

This section deals with the fabrication recipe of chip MP549\_2 and general instructions concerning the fabrication process. A difference to previous fabrication methods with VLS grown nanowires is the lack of *blanks*, chips with previously deposited gold bonding pads<sup>4</sup>, leads and alignment marks where nanowires are deposited with a micromanipulator before fabrication. These structures have to be designed, exposed and deposited on every new SAG die individually, which leads to an increase in design and exposure time. Once a design is created and the parameters as aluminum deposition direction, position and orientation of the nanowires remain unchanged it allows for reuse of the prepared design and a fast fabrication of measurable samples.

### 5.4.1 Step 0: Design preparation and other prefabrication steps

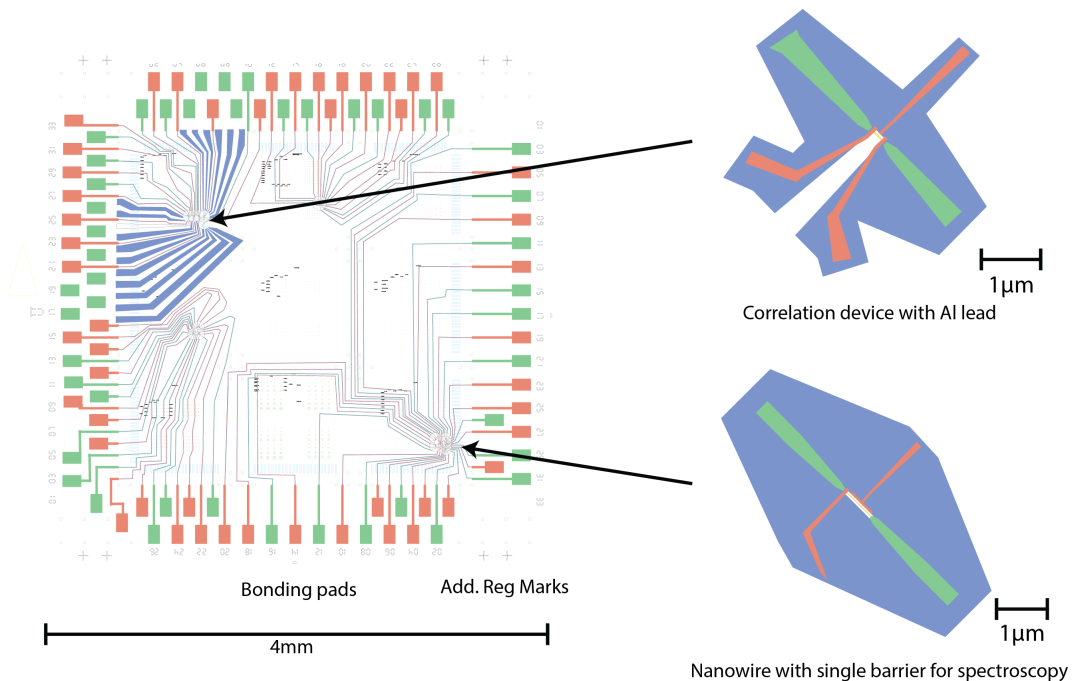


Figure 5.5: Left: Final design of Chip Mp548\_2. Red corresponds to gates, green to contacts and blue marks the aluminum etch. The blue etching windows in the top left area of the chip are used to create aluminum leads. Bonding pads on the bottom left of the designs are redistributed because of a nudge in the chip border. Top right: Three terminal device with two normal leads with barriers, one Al lead and a gate to tune density. Bottom right: Single nanowire with one barrier for one sided tunnel spectroscopy

First step in the fabrication process is the preparation of the design. This includes the devices itself around the semiconductor structures and lines leading from these connection to the bonding pads. Important details in preparation are the deposition direction of the aluminum to choose the correctly oriented structures on the chip, where the deposition direction is orthogonal to the main wire axis direction. When using side gates, they have to be placed on the opposite side of the wire to prevent screening from the aluminum facet. On wafers with varying quality of SAG structures it is advised to investigate

<sup>4</sup>larger metallic surfaces used to connect the chip to the fridge and the measurement set up

appropriate structures optically and design on the most promising ones to increase yield. In extreme cases it is beneficial to investigate different chips of the growth with a scanning electron microscope for pre-selection.

Gates should be separated by 80nm and more in design to avoid failures during lift off. The edge of the leftover aluminum after etch should be at least 100nm separated from contacts to avoid direct connection of the two. Aluminum etching windows should account for the previously determined overetch.

To determine the quality of the etch more precisely, it is possible to also insert etching windows on unused structures to investigate the etch after metal depositions without metallic structures covering the leftover aluminum.

To save exposure time, the design is split into finer features (everything in a  $25\mu\text{m}$  radius around each device) and rougher features (lines and bonding pads). Inner features can then be exposed at a lower beam current for higher precision while outer features can be exposed at higher beam current and are separated in space from critical features to avoid overexposure.

The lines leading to the devices should not cross any grown semiconductor structures.

#### 5.4.2 Step 1: Aluminum etch

The aluminum plane covering the entire wafer has to be removed around the gold lines leading to contacts and gates and bonding pads to avoid electrical contact between different lines (*shorts*). Because of the size of the area, the etching process is separated into a two step process to decrease exposure time.

First step: Aluminum etching windows and leads

1. Spin Resist El9 (MMA) at 4000RPM for 45 seconds and bake on a heat plate for 2 minutes. Check uniformity of the resist layer under optical microscope.
2. EBL is done in a *Elionix ELS-7000*. Expose inner features at  $280\ \mu\text{C}/\text{cm}^2$ ,  $300\ \mu\text{m}$  write fields, 300 dots and 500pA beam current and outer features at  $400\ \mu\text{C}/\text{cm}^2$  and 20nA beam current.
3. Develop 30 seconds in 1:3 methyl isobutyl ketone (**MIBK**) isopropyl alcohol (**IPA**) and rinse for 10 seconds in pure IPA. Blow dry with nitrogen gun. Check quality of development under optical microscope.
4. Ash in in an oxygen plasma asher for 60s to remove leftover resist and activate surface.
5. Bake at  $125^\circ\text{C}$  for 1 min.
6. Etch in *Transene ALUMINUM ETCHANT – TYPE D* at  $50^\circ\text{C}$  for 8s, rinse in  $50^\circ\text{C}$  *Milli-Q* water for 5 seconds, and then rinse in room temperature *Milli-Q* water for 20 seconds. Check quality of etch under optical microscope.
7. Remove resist in dioxolane for 15 minutes.

Second step: Area surrounding bonding pads.

1. Spin photo resist *MZI505* at 4000RPM for 45 seconds and bake on a heat plate for 2 minutes. Check uniformity of the resist layer under optical microscope with yellow light filter.
2. Expose pattern in *Heidelberg instruments  $\mu$ PG 101*.
3. Develop in *AZ-developer* for 60s. Rinse in *Milli-Q* water for 15 seconds. Check quality of development under optical microscope with yellow light filter.
4. Ash in in an oxygen plasma asher for 60s to remove leftover resist and activate surface.
5. Bake at 125°C for 1 min.
6. Etch in *Transene ALUMINUM ETCHANT – TYPED* at 50°C for 15s, rinse in 50°C *Milli-Q* water for 5 seconds, and then rinse in room temperature *Milli-Q* water for 20 seconds. Check quality of etch under optical microscope.
7. Remove resist in Acetone for 15 minutes.

#### 5.4.3 Step 2: Titanium-Gold contacts

1. Spin Resist 50k (PMMA with reduced molecular weight) at 4000RPM for 45 seconds and bake on a heat plate for 2 minutes.
2. Spin Resist 50k (PMMA with reduced molecular weight) at 4000RPM for 45 seconds and bake on a heat plate for 2 minutes.
3. Spin Resist A6 (PMMA) at 4000RPM for 45 seconds and bake on a heat plate for 2 minutes. Check uniformity of the resist layer under optical microscope.
4. Expose inner features at 920  $\mu\text{C}/\text{cm}^2$ , 300 $\mu\text{m}$  write fields, 300 dots and 500pA beam current and outer features at 1300  $\mu\text{C}/\text{cm}^2$  and 20nA beam current.
5. Develop 60 seconds in 1:3 MIBK IPA and rinse for 10 seconds in pure IPA. Blow dry with nitrogen gun. Check quality of development under optical microscope.
6. Ash for 60s.
7. Mill with Kaufmann ion milling source for 8 minutes to remove native oxide layer from nanowires and enable electrical contact. Deposit 5nm of Ti as a sticking layer and 110nm of Au in a thin film deposition chamber at 1  $\text{\AA}/\text{s}$ .
8. Liftoff in 55°C dioxolane for 35 minutes, blow away excess gold with a pipette in solution, rinse in Aceton for 10 seconds and IPA for 10 seconds. Before blow drying the sample check liftoff under optical microscope in IPA. If liftoff is not complete, repeat. Otherwise, blow dry sample with nitrogen gun.

#### 5.4.4 Step 3: Oxide layer

1. Load sample into atomic layer deposition (ALD) chamber. Pump for 10 hours to degas the sample. Deposit 6nm of HfO on the chip, at a rate of 1nm per hour.

#### 5.4.5 Step 4: Titanium-Gold gates

1. Spin Resist 50k (PMMA with reduced molecular weight) at 4000RPM for 45 seconds and bake on a heat plate for 2 minutes.
2. Spin Resist A4.5 (PMMA) at 4000RPM for 45 seconds and bake on a heat plate for 2 minutes. Check uniformity of the resist layer under optical microscope.
3. Expose inner features at  $920 \mu\text{C}/\text{cm}^2$ ,  $300\mu\text{m}$  write fields, 300 dots and 500pA beam current and outer features at  $1300 \mu\text{C}/\text{cm}^2$  and 20nA beam current.
4. Ash for 60s.
5. Deposit 5nm of Ti as a sticking layer and 100nm of Au in a thin film deposition chamber at  $1 \text{ \AA}/\text{s}$ .
6. Liftoff in  $55^\circ\text{C}$  dioxolane for 35 minutes, blow away excess gold with a pipette in solution, rinse in Aceton for 10 seconds and IPA for 10 seconds. Before blow drying the sample check liftoff under optical microscope in IPA. If liftoff is not complete, repeat. Otherwise, blow dry sample with nitrogen gun.
7. Take final images in a SEM.

## 5.5 Measurement setup

### 5.5.1 Two vs. three terminal measurement

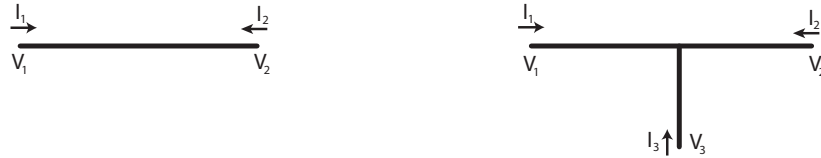


Figure 5.6: Models of a two terminal and a three terminal measurements. Current directions are depicted at every lead.

VLS wires are typically measured in a two terminal measurement where one side is biased with AC and DC bias and drained through the other side. The aluminum facet is hard to contact without introducing disorder into the system. SAG allows for the opportunity to use the superconducting plane as another terminal and to expand the system beyond the two terminal geometry. Expanding your system from two to three terminals is not as trivial as one might think. Considering the conductance matrices shows quickly why (technical current directions are introduced in Figure 5.7). In the two terminal case one receives

$$G_{2T} = \begin{pmatrix} G_{1,1} & G_{1,2} \\ G_{2,1} & G_{2,2} \end{pmatrix} = \begin{pmatrix} \frac{dI_1}{dV_1} & \frac{dI_2}{dV_1} \\ \frac{dI_1}{dV_2} & \frac{dI_2}{dV_2} \end{pmatrix} \quad (29)$$

Because of conservation of current  $I_1 = -I_2$  holds which reduces the matrix to two variables from which the complete matrix can be inferred. Additionally arising from the gauge invariants of the Maxwell Equations, the potentials are only valid up to a constant. This allows us to rewrite our conductance matrix in terms of the potential difference  $\Delta V = V_1 - V_2$ . In an experimental setup  $V_2$  is simply held at 0 by grounding for convenience. This leads to the following transformation

$$\frac{dI_1}{dV_2} = \frac{dI_1}{dV_2} \underbrace{\frac{d\Delta V}{d\Delta V}}_{=1} = \frac{dI_1}{d\Delta V} \underbrace{\frac{d\Delta V}{dV_2}}_{=-1} = -\frac{dI_1}{d\Delta V} \quad (30)$$

$$G_{2T} = \begin{pmatrix} \frac{dI_1}{d\Delta V} & -\frac{dI_1}{\Delta V} \\ -\frac{dI_1}{d\Delta V} & \frac{dI_1}{\Delta V} \end{pmatrix} \quad (31)$$

leaving behind only one independent quantity to be measured  $\frac{dI_1}{d\Delta V}$ . In the three terminal case, there are nine conductances to be considered in the general case:

$$G_{3T} = \begin{pmatrix} G_{1,1} & G_{1,2} & G_{1,3} \\ G_{2,1} & G_{2,2} & G_{2,3} \\ G_{3,1} & G_{3,2} & G_{3,3} \end{pmatrix} = \begin{pmatrix} \frac{dI_1}{dV_1} & \frac{dI_2}{dV_1} & \frac{dI_3}{dV_1} \\ \frac{dI_1}{dV_2} & \frac{dI_2}{dV_2} & \frac{dI_3}{dV_2} \\ \frac{dI_1}{dV_3} & \frac{dI_2}{dV_3} & \frac{dI_3}{dV_3} \end{pmatrix} \quad (32)$$

Conservation of current  $I_1 + I_2 = -I_3$  implying  $\frac{dI_1}{dV_x} + \frac{dI_2}{dV_x} = \frac{dI_3}{dV_x}$  and the introduction of two potential differences  $\Delta V_{1,3} = V_1 - V_3$  and  $\Delta V_{2,3} = V_2 - V_3$

$$G_{3T} = \begin{pmatrix} \frac{dI_1}{d\Delta V_{1,3}} & \frac{dI_2}{d\Delta V_{1,3}} & -\left(\frac{dI_1}{d\Delta V_{1,3}} + \frac{dI_2}{d\Delta V_{1,3}}\right) \\ \frac{dI_1}{d\Delta V_{2,3}} & \frac{dI_2}{d\Delta V_{2,3}} & -\left(\frac{dI_1}{d\Delta V_{2,3}} + \frac{dI_2}{d\Delta V_{2,3}}\right) \\ -\frac{dI_1}{d\Delta V_{1,3}} & -\frac{dI_2}{d\Delta V_{2,3}} & \left(\frac{dI_1}{d\Delta V_{1,3}} + \frac{dI_2}{d\Delta V_{2,3}}\right) \end{pmatrix} \quad (33)$$

This leaves four independent quantities from which the complete conductance matrix can be inferred: two local conductances on the diagonal:  $\frac{dI_1}{d\Delta V_{1,3}}$ ,  $\frac{dI_2}{d\Delta V_{2,3}}$  and two nonlocal conductances (off-diagonal):  $\frac{dI_2}{d\Delta V_{1,3}}$ ,  $\frac{dI_1}{d\Delta V_{2,3}}$ .

### 5.5.2 Voltage divider

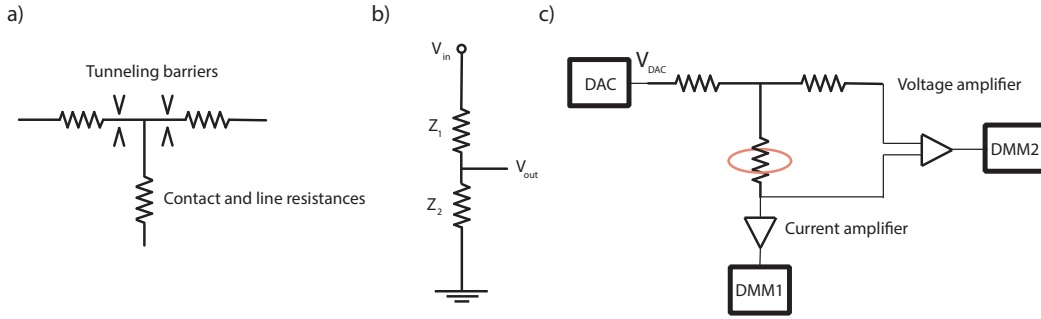


Figure 5.7: a) Advanced three terminal model with contact resistances on each arm and two tunneling probes. b) Schematic of a voltage divider with two resistances, one ( $Z_1$ ) in series between in and output potential and the other one ( $Z_2$ ) leading to ground. c) Measurement setup to measure the contact resistance of one lead (red circle) by applying a known current and measuring voltage drop over the contact resistance. Resistance is extracted by Ohm's law. This scheme is repeated for all three leads. Dilution refrigerator not depicted for simplicity.

In the next step our three terminal toy model is equipped with ohmic resistances on all arms and two tunnel probes (see Figure 5.7a). This is motivated that cryogenic measurements usually carry line resistances due to filters used to reduce noise and avoid high temperature electrons warming up the sample. At the tunnel probes charge carriers are expelled from this part of the semiconducting wire to create an insulating region using a negative electrostatic potential. In the regime of equal conductances on all three arms (tunnel probes with low potentials, *open regime*) voltage division effects in conductive measurements become visible. Voltage dividers are a two resistor network depicted in Figure 5.7b. It divides an incoming voltage  $V_{in}$  by the following equation:

$$V_{out} = \frac{Z_2}{Z_1 + Z_2} \times V_{in} \quad (34)$$

quickly verifiable by Ohm's law. This concept is usually used beneficially as it allows for higher resolutions of measurement equipment when applying potentials to our system by dividing the applied voltages before routing them to the sample. We measure differential current running through our sample to probe the density of states in the sample.

This is done by sweeping the voltage bias applied on one side of the tunneling barrier, only allowing differential current when on resonance with another state on the other side of the barrier. In the open regime the resistances of the tunneling probes are negligible and our line resistances are more or less equal. The resistances on each arm have been measured individually in the configuration with open tunnel probes depicted in Figure 5.7.c and show that all resistances are comparable around 8.4 k $\Omega$ , including the 5.7 k $\Omega$  line resistance coming from resistors used in cryogenic filters and on the motherboard. In the open regime, small changes in tunnel probe resistances lead to a significant voltage drop of our applied voltage over the line resistances. This affects tunneling spectroscopy as the bias on the tunneling barrier is not the bias we apply at the fridge. When closing the tunnel probes the system enters the so called *tunneling regime*, where current running is only mediated over tunneling processes across the barrier. The resistances of the tunnel probes become 250 k $\Omega$  and above which render the effect of the voltage division negligibly small. Our models show that below a conductance of  $0.1 e^2/h$  which corresponds to a resistance of 250 k $\Omega$  less than 2% of our applied voltage drops over the line resistances. The open regime is therefore avoided and the effect of voltage divider effects as a cause for induced correlations in our measurement has been studied (see Appendix).

### 5.5.3 Measurement Setup

Leading from these measurement challenges, the following setup is used to take our measurement data (Figure 5.8).

The sample is placed in a *Blue Fors Quick Test Dilution Refrigerator* and cooled to base temperature (20 mK), equipped with RC-RF filters on each line leading down to the sample to filter out high frequency noise. One lead gets grounded at the fridge to set its potential to zero while the other two leads get connected to two *Basel Low Noise Low Impedance Current Amplifier*. These convert running current into voltage and amplify by a variable factor (this factor is set by the resistance of our feedback resistor - in this case  $10^7 \Omega$ ). These transimpedance amplifiers provide an additional port to voltage bias the sample with a built in division factor of 1:100 for incoming signals. To increase this division factor, a home-build resistor network is placed in series to allow for mixing of AC and DC excitations and increase the division factor to 1:89000 for AC and 1:1007 for DC signal (measured individually). AC excitations are provided by two *Stanford Research SR860* lock-ins (lock-in 1, lock-in 3) with carrier signals at two frequencies  $f_1 = 28$  Hz and  $f_2 = 38$  Hz with amplitude of 1V, chosen to be at beneficial frequency windows with low noise background, measured by a spectrometer. This gives an excitation amplitude after the voltage division of 11  $\mu$ V at the sample. It is overlaid with a DC signal provided by a custom built 16bit digital-to-analog converter (DAC). The outgoing signal is routed back from the current amplifiers to the lock-ins, measuring the two local conductances  $\frac{dI_L}{d\Delta V_L}$ ,  $\frac{dI_R}{d\Delta V_R}$  by digitally dividing the measured current with the applied voltage. The nonlocal conductances  $\frac{dI_R}{d\Delta V_L}$ ,  $\frac{dI_L}{d\Delta V_R}$  are measured by two additional lock-ins (lock-in 2, lock-in 4). Each of them is frequency locked to one of the lock-ins providing the excitation signals and use their internal clock as a reference for incoming signals (*slaved*). They measure the running current on the opposite terminal of their respective excitation frequency, providing the other two conductances of our conductance matrix. Density of the semiconductor wire can be con-

trolled by capacitively coupled metal gates, controlled also by the DAC. All measurement equipment is coordinated by the *QCoDeS* suite.

#### **5.5.4 Noise reduction**

To reduce noise in our measurements these points have been accounted for:

1. All measurement equipment is connected to the same ground. In general ground loops which pick up electromagnetic noise are identified and eliminated before measurement.
2. High noise measurement equipment like the measurement computer and power supplies are separated in space far from noise sensible equipment like the current amplifiers and lock-ins.
3. Remove unused equipment from the rack or at least disconnect them from power if possible.
4. Choose lock-in excitation frequencies at low noise windows (50Hz and multiples are unfit because of the AC-excitation of the Danish power system).

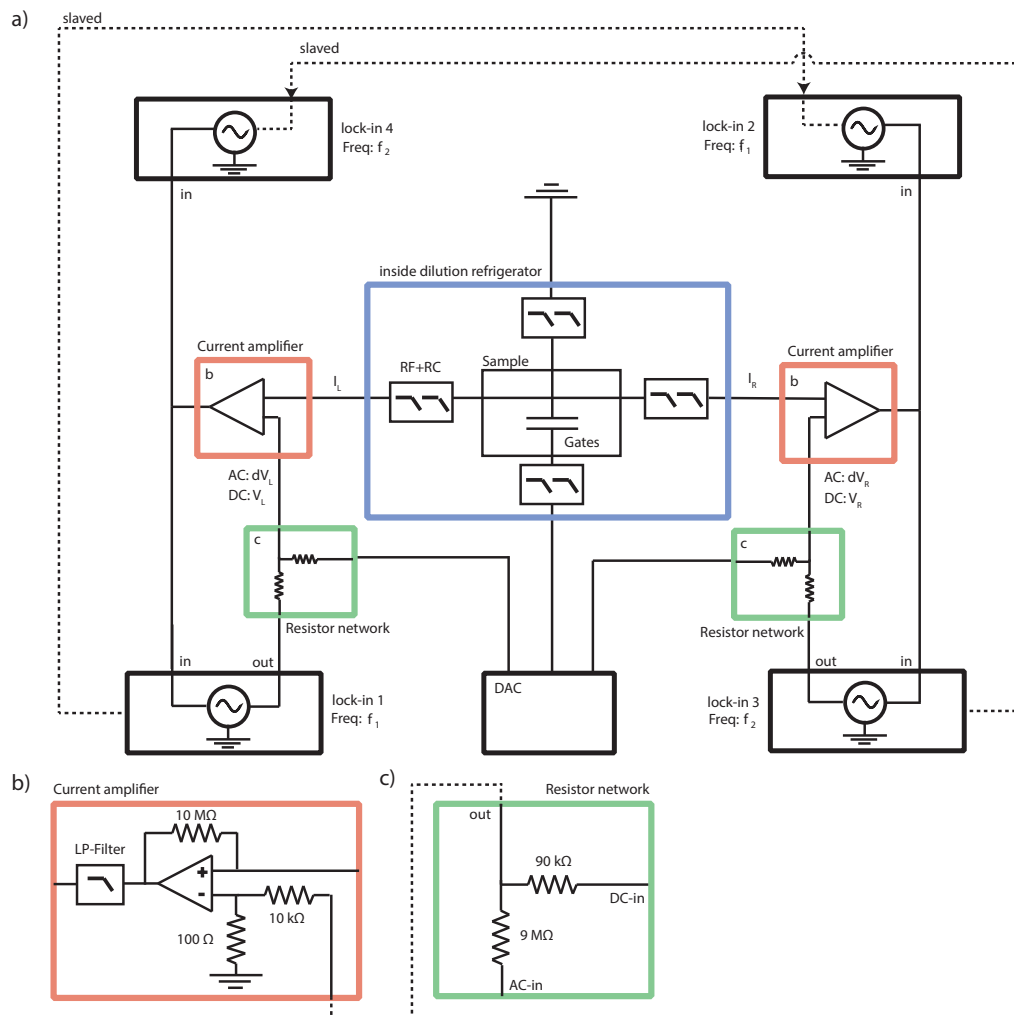


Figure 5.8: a) Diagram of the measurement setup for a three terminal device. AC-excitation is provided by lock-in 1 and 3, mixed with a DC-offset provided by the DAC and routed to the bias input of the two current amplifiers. The current amplifiers measure running current on both sides, converting it to voltage and amplifying it by a chosen factor. It gets routed to all four lock-ins to measure all independent conductances, related to a given energy spectrum at the chosen DC-offset configuration. Sweeping DC offset provides insight into the whole energy spectrum of the wire.

## 6 Results

The possibility of being able to grow nanowire networks beyond the two terminal geometry opens up a range of experiments stretching from interferometers [50] over braiding experiments to scalable qubit architectures. As this is new material and our understanding of it still limited the first experiments on this start small and careful.

Tunneling spectroscopy is a useful tool for probing the density of states of nanowires [51] and giving insight into the behavior of the superconducting gap and subgap states. The catch is that it only gives insight into the local density of states in the vicinity of the tunneling barrier and does not reveal information about the bulk of the wire [52]. Even if the probed system would correspond to Majorana zero modes with non-abelian statistics, it is not clear if the topological phase extends over the whole length of the wire, which is a requirement for further experiments. The topological phase can be interrupted by trivial phases through disorder of the wire or a faulty interface between superconductor and semiconductor. The idea of this experiment is to probe both sides of a nanowire by tunneling spectroscopy simultaneously by introducing a third lead between the two tunneling probes. If subgap states or a possible topological phase extend over the entire length of the wire, the spectroscopy on both sides should couple to the same subgap states and show similar density of states, with similar dependencies on electric fields and applied magnetic fields. This three terminal geometry with two normal leads and one superconducting lead is also used as a Cooper pair splitter [53, 54], where entangled electrons are created via the superconducting pairing relation promising applications in quantum computing and quantum information processes.

The devices are fabricated on a SAG die grown by the group around Chris Palmstrøm in Santa Barbara. Base wafer is a InP wafer capped with SiO, semiconducting buffer layer consists of InAsP topped by the InAs nanowire. Two of the three contacts are normal leads made from 110 nm thick Au with a sticking layer of 5 nm of Ti. The third contact is made from the epitaxial Al. By the previously described wet etch technique the excess Al is removed from the device besides one plane of 10 nm thickness covering one facet of the buffered nanowire and a conductive channel leading to the outer bonding pads. This superconducting lead is only possible in SAG and not with the conventional grown nanowires as it is deposited in situ. No milling is necessary to remove native oxide which would introduce disorder and degrade the quality of the material. Au gates of 90 nm thickness are separated by a 6 nm thick insulating layer of HfO from the conductive channel. The thin gates covering the wire are used to deplete the wire below from charge carriers creating a potential barrier (*Pinchers*). The gate positioned on the side of the wire is used to tune the chemical potential of the semiconductor (*Plunger*). The two devices depicted differentiate in the length in between the two tunneling probes. For device 1 which most measurements in this segment are done on they are separated by 300 nm and for the long device 2 by 900nm.

### 6.1 Tuning into the double tunneling regime

At the beginning of the measurement the two sides are tuned separately into the tunneling regime. In this first measurement our setup is slightly altered: we apply the AC and

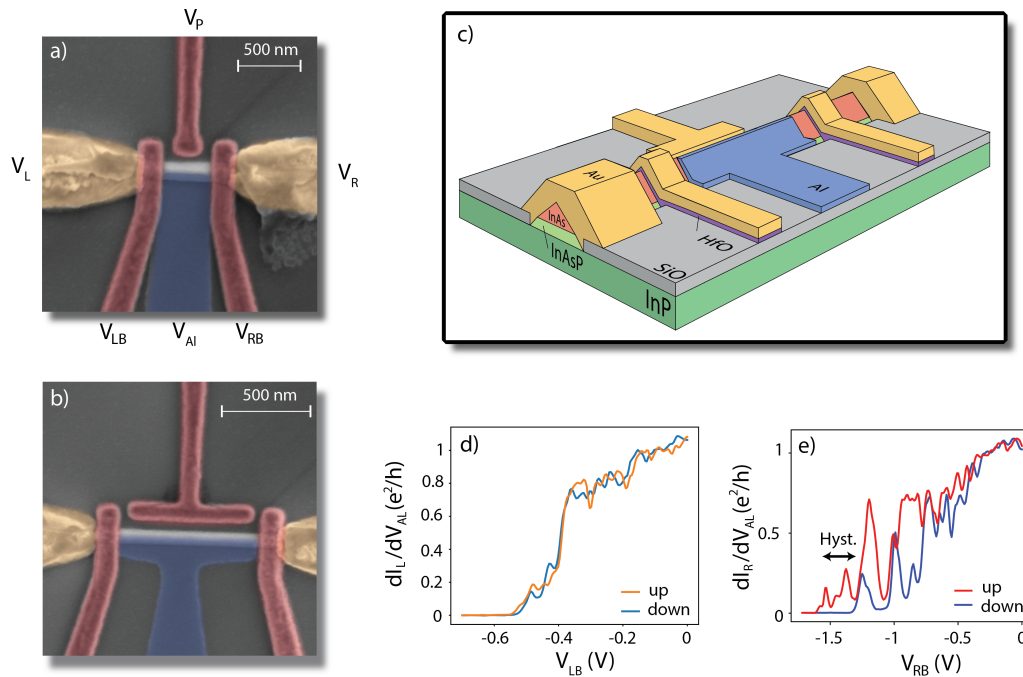


Figure 6.1: a) 300nm long three terminal device with two normal leads (yellow) and one superconducting lead (blue), gates to tune density and create tunneling probes are colored red. b) 900nm long three terminal device from the same fabrication process as the first device located on the same die. c) Schematic of the two devices highlighting material composition. d) Up and down Pinchoff curve for the left barrier, right barrier open e) Up and down Pinchoff curve for the right barrier, left barrier open

DC excitations at the aluminum lead and measure the two local conductances with two lock-ins on one carrier frequency on both sides. As we previously defined our system by voltage differences between the super lead and the two normal leads this does not lead a difference in local conductances (see Appendix Figure A.1), it just does not allow for the measurement of the nonlocal conductances. By sweeping the potential ( $V_{LB}$  or  $V_{RB}$ ) of the respective gate, charge carriers are removed from the underlying part of the nanowire. The other potential sides stays fixed at zero. Conductance drops over the range of 0.6V from  $1.2$  to  $0 e^2/h$  (Figure 6.1d) for the left barrier on the left side and over 1.6V for the right barrier on the right side (Figure 6.1e). These traces are taken at out of gap DC-bias. The right barrier goes through a number of resonances while pinching off. In the continuing measurement it is carefully avoided to cross these resonances during a measurement with changing potential on the right barrier. Opening and closing the potential barriers leads to a slightly shifted curve in conductance, this is referred to as *hysteresis*, visible on the right barrier where the two curves are shifted by 0.2 V. It is possibly related to a charge carrier redistribution to the new potential landscape after a potential sweep.

A measurement of  $dI_{L/R}/dV$  while closing the potential barriers versus sweeping the DC-bias on the same side is depicted in Figure 6.2a,c. It shows a crossover from a transmissive regime with high conductance ( $1 e^2/h$ ) at low bias to a tunneling regime with low conductance at low bias, revealing the superconducting density of states with the characteristic gap and some subgap states. This confirms that the nanowire is proximitized by

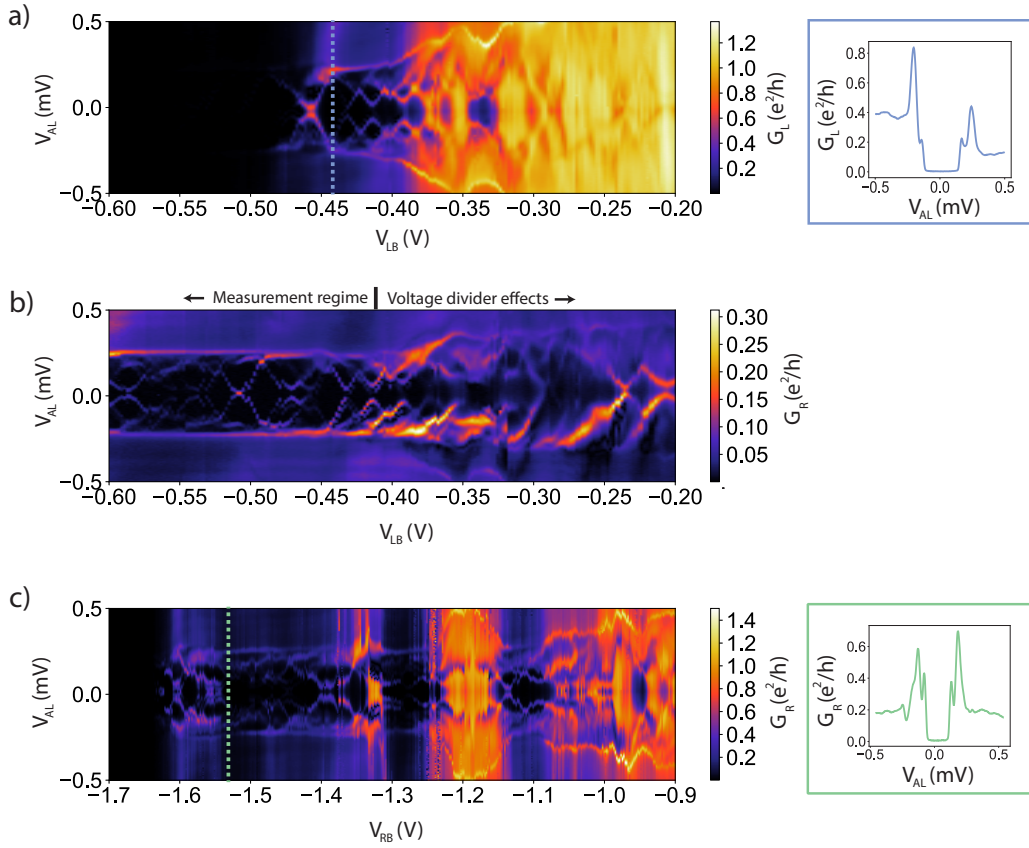


Figure 6.2: a) Differential conductance  $dI_L/dV_{Al} = G_L$  in dependence of the potential on the left barrier  $V_{LB}$  and bias  $V_L$ . Inset shows a cut at the blue dashed line to show the superconducting density of states. b) Differential conductance  $dI_R/dV_{Al} = G_R$  in dependence of the potential of the left (opposite) barrier and bias. Data is taken simultaneously to a) at  $V_{RB} = -1.45$  V. c) Differential conductance  $dI_R/dV_{Al}$  in dependence of the potential on the left barrier  $V_{RB}$  and bias  $V_L$ . Inset shows a cut at the green dashed line to show the superconducting density of states.

the Al facet. The left side is entering the tunneling regime at  $V_{LB} = -0.4$  V and the right side is entering it at  $V_{LB} = -1.1$  V. Here the resonances previously found in the 1D pinch off curve appear as stripes of increased conductance in the measurement of the right conductance. The insets in Figure 6.2 a,c show cuts at the marked places showing the superconducting gap on both sides with  $\Delta = 235$   $\mu$ eV in peak to peak voltage. The hardness of the superconducting gap probed on one side has been studied in dependence of the 'openness' of the other tunneling barrier. In Figure 6.2b the gap is probed in dependence on the applied potential of the other tunneling barrier. This data is taken at the same time as the data from plot a) so one can follow the openness of the other barrier in the picture above. As long as the left tunneling barrier has not entered tunneling regime ( $V_{LB} > -0.4$  V), voltage division effects are visible. In this regime, a significant part of our applied bias potential drops over the line and contact resistances leading to the effect that the resonances probed in the tunneling spectroscopy happen at factors  $>1$  of the  $V_{Al}$  resulting in a stretched image. After entering tunneling regime, the gap is observed at a constant  $V_{Al}$ . Subgap states are being tuned by the cross talk of the two barriers even without changing  $V_P$  because of the

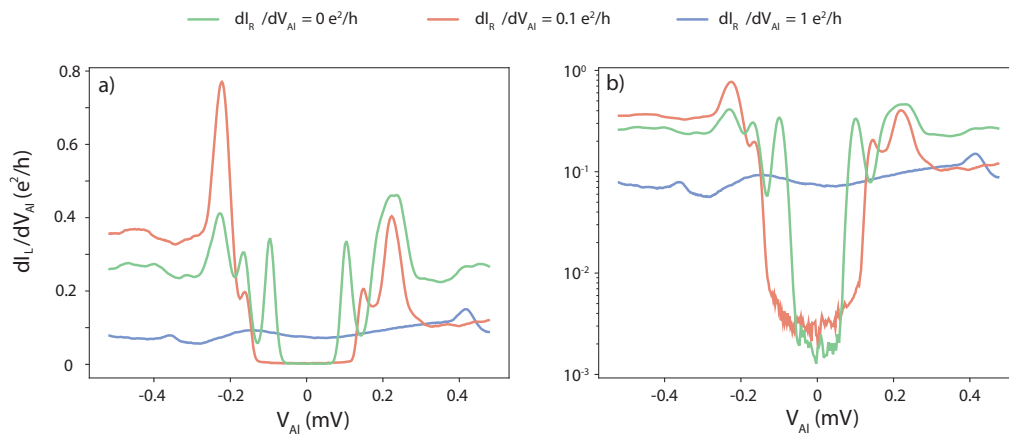


Figure 6.3: Superconducting gap of the left tunneling probe in three configurations of the right tunneling probe. Green corresponds to the completely closed regime of the right barrier, red the tunneling regime and blue is completely open. a and b show the same data with a linear/logarithmic differential conductance axis.

small separation in real space. In Figure 6.3 three cuts of the left differential conductance at different conductances of the right barrier have been plotted on a linear (a) and a logarithmic (b) scale. When pinching off the right barrier the superconducting gap is visible and for the completely pinched off regime the in-gap conductance at zero bias slightly lowers further. The visible subgap states are tuned by the cross talk of the two barriers even if this cuts have been taken at the same value of  $V_{LB}$ . In contrast, when the right barrier is tuned into the transmissive regime ( $dI_R/dV_{Al} \sim 1e^2/h$ ) no gap is observed on the left hand side. Evidently this constitutes a broadening of the left local density of states by coupling to normal electrons of the right lead, an effect which has not been previously reported in the literature.

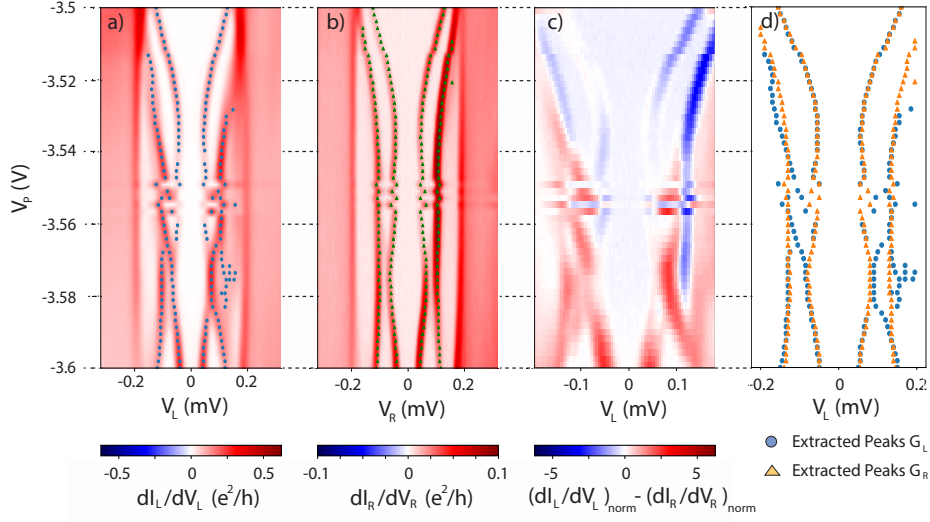


Figure 6.4: a) Local differential conductance  $dI_L/dV_L$  in dependence of Plunger potential  $V_p$  and left side bias  $V_L$ . Extracted peak positions are represented by markers. b) Local differential conductance  $dI_R/dV_R$  in dependence of Plunger potential  $V_p$  and right side bias  $V_R$ . Extracted peak positions are represented by markers. c) Normalized conductance of a) subtracted by the normalized conductance of b) reduced to the inside of the gap. d) Extracted peak positions from a and b layered on top of each other to show match or mismatch.

## 6.2 Two sided tunneling spectroscopy

After tuning into the tunneling regime, the gates are position at the marked barrier values in Figure 6.2 and the measurement setup is switched to the one described in 5.8. Now by sweeping  $V_p$ , the density inside the nanowire is tuned and the variety of subgap states is studied. One measurement consists of eight different conductances:  $\frac{dI_L}{d\Delta V_L}(V_L)$ ,  $\frac{dI_R}{d\Delta V_L}(V_L)$ ,  $\frac{dI_L}{d\Delta V_R}(V_L)$ ,  $\frac{dI_R}{d\Delta V_R}(V_L)$ ,  $\frac{dI_L}{d\Delta V_L}(V_R)$ ,  $\frac{dI_R}{d\Delta V_L}(V_R)$ ,  $\frac{dI_L}{d\Delta V_R}(V_R)$ ,  $\frac{dI_R}{d\Delta V_R}(V_R)$ . These are taken by sweeping  $V_L$  at the given fixed configuration of gates and field to record the behavior of the device under spectroscopy from the left side and keeping  $V_R$  at zero while measuring the previously discussed  $dI/dV$ s. Then  $V_L$  is fixed at zero bias and the other side is swept (All conductances from one cut are plotted in the Appendix B.3). After this the gate configuration is incrementally stepped and all eight conductances are retaken. In Figure 6.4 a,b the  $\frac{dI_L}{d\Delta V_L}(V_L)$  and  $\frac{dI_R}{d\Delta V_R}(V_R)$  are shown over a small range of  $V_p$ . Two subgap bands are visible in this regime on both sides. By eye, they show similar behavior.

To compare the coupling strength of the observed states to the two sides, both sides are normalized by their out of gap conductance and subtracted from each other in Figure 6.4c. This reveals that some states are more strongly coupled to the right side (blue) and some are more strongly coupled to the left side (red). Coupling strength of a single state also changes depending on the position in plunger gate space.

The positions of the sup gap states in bias-plunger space are extracted by a peak-

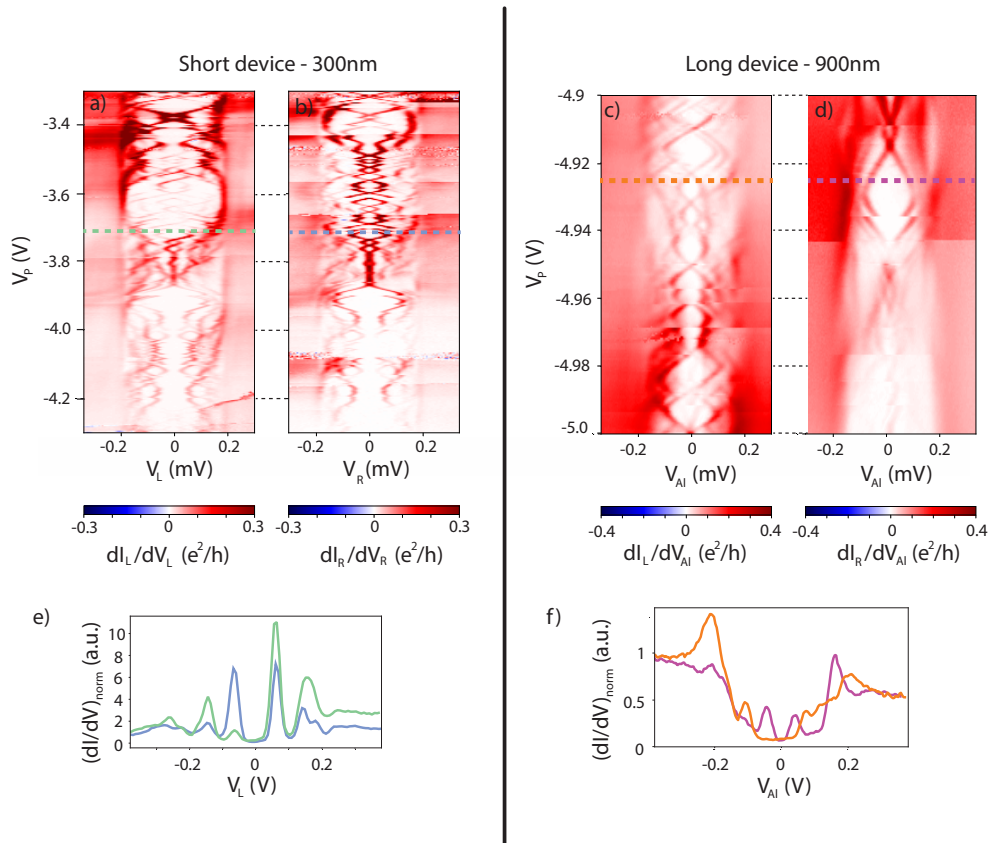


Figure 6.5: a) Local differential conductance  $dI_L/dV_L$  in dependence of plunger potential  $V_P$  and left side bias  $V_L$  of the 300nm device. b) Local differential conductance  $dI_R/dV_R$  in dependence of Plunger potential  $V_P$  and right side bias  $V_R$  of the 300nm device. c) Local differential conductance  $dI_L/dV_L$  in dependence of Plunger potential  $V_P$  and bias  $V_{Al}$  of the 900nm device. d) Local differential conductance  $dI_R/dV_R$  in dependence of Plunger potential  $V_P$  and bias  $V_{Al}$  of the 900nm device. e) Cuts at the marked position of a and b. f) Cuts at the marked positions of c and d.

finding algorithm and are marked in both plots a and b. Plotting this peak positions of both sides in one graph (Figure 6.2d) shows that they indeed follow similar trajectories. At  $V_P$  -3.56 V the left side observes a crossing between the two states while the right side observes them separated. Another thing to highlight is that the *switches*, sudden changes in the behavior of the device during measurement, in the middle of the measurement are visible on both sides.

To be able to quantify correlation over statistical methods, in Figure 6.5a,b the same measurement is taken over a wider ranger of  $V_P$ . In this measurement a similar qualitative picture as previously is observed. The states follow a similar trajectory but with a different coupling strength to both sides. This becomes more apparent in the cut taken at the marked position in Figure 6.5e). In the range between between -3.3 V and -3.9 V the ABS cross zero energy, hinting that these states might be associated with charging energy.

On the contrary in Figure 6.5c,d a similar data set taken from the 900nm device shows a qualitatively different picture. This data set is also taken with the DC and AC excitation applied to the superconducting lead, because the long device became unresponsive be-

fore we could switch to the final measurement setup. As previously mentioned, this gives the same results for the local conductances but for comparison reasons the exact same measurement setup on both setups would have been preferable. There are subgap states present on both sides of the device but they follow different trajectories. The switches during measurement do not happen at similar values of  $V_P$ . Cuts at the same value of  $V_P$  highlight the different peak spacing 6.5. These subgap states also cross zero energy.

To have a more sophisticated approach in viewing correlation between the two sides than comparing both sides by eye, statistics of the states are extracted by the following scheme: Subgap states are identified by the peak-finding algorithm mentioned previously. At this identified positions, the normalized conductance of the right side  $G_{R,peak,norm}$  is divided by the normalized conductance  $G_{L,norm}$  of the same position in  $V_P - V_L$  space on the left side. The arctangent of this measure spaces these weights between 0 and  $\pi/2$ . Perfectly correlated values with equal coupling between both sides are located in this representation as a peak around  $\pi/4$  while uncorrelated states tend to move towards the edge of this distribution at 0 (state only present at the left side) and  $\pi/2$  (state only present at the right side).

$$C = \arctan\left(\frac{G_{R,peak,norm}}{G_{L,norm}}\right) \quad (35)$$

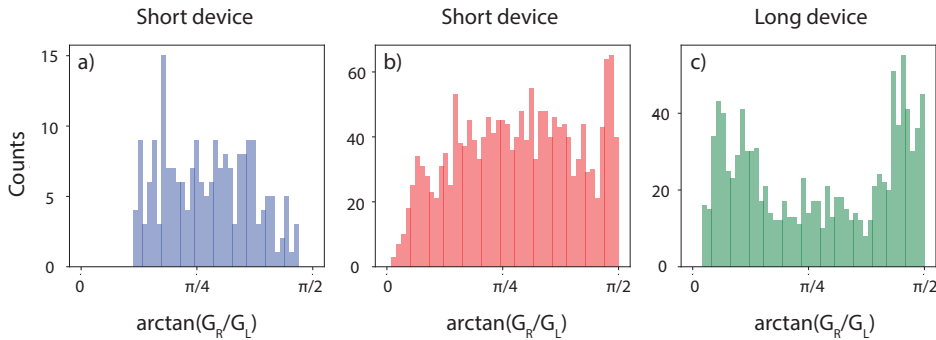


Figure 6.6: a) Histogram of the correlation angle made from the small range datasets for the short device from Figure 6.4a,b. b) Histogram of the correlation angle made from the long range datasets for the short device from Figure 6.5a,b. c) Histogram of the correlation angle made from the short range datasets for the long device from Figure 6.5c,d.

The distributions of this correlation angle  $C$  for the three presented data sets above are depicted in Figure 6.6. Both 300 nm datasets show distributions that are roughly uniform from 0 (left side coupled) to  $\pi/2$  (right side coupled). In other words states are as likely to be coupled to be symmetrically coupled to the leads as they are asymmetrically coupled to the leads. This observation implies that the Andreev bound states are delocalized on a 300nm length scale.

In contrast gives a distribution with strong peaks at 0 (left side coupled) and at  $\pi/2$  (right side coupled). Evidently, in the 900nm device states are drawn from a distribution that are associated with one end of the device or the other. This observation implies that the ABS are localized in the 900nm device

The visible correlations in the 300 nm device hints that it is placed in the  $L/2 < \xi$  regime

---

where ABS can extend on a length scale that they couple to both tunneling probes. The missing correlation on the 900 nm device strongly indicates that here  $L/2 > \xi$  holds. This sets an upper boundary for the coherence length of the hybrid system probably caused by disorder in the system that could be related to the amount of ABS we observe in our gap. One interpretation of this data is that one or two accidental quantum dots (similar to Deng *et al.* [42]) are present in the constrictions for both devices which coupled to the superconductor cause these ABS. The ABS crossing zero energy also hints at a an object with charging energy present in the system as charging energy is the main mechanism we are aware of that pushes ABS through zero [55]. This object might be a potential well localizing ABS at its position or a quantum dot in the constriction. In the short device the small separation in space would still allow both normal leads to couple to both dots/wells while in the long device the local density of states probed by the tunneling probes are separated over more than the length of the superconducting coherence length essentially decoupling both leads.

### 6.3 Nonlocal conductances

As previously discussed, tunneling spectroscopy does not provide conclusive evidence if a system enters the topological phase [40, 39]. Trivial ABS can mimic the zero bias conductance signature below the topological phase transition. A different criterion is necessary to distinguish these excitations from each other. One criterion is found in the nonlocal conductance behaving characteristically at the topological phase transition [52]. This motivates us besides the predicted signature of ABS in a three terminal measurement from Section 3.4.2 and the measurement of a full conductance picture to record the nonlocal conductance.

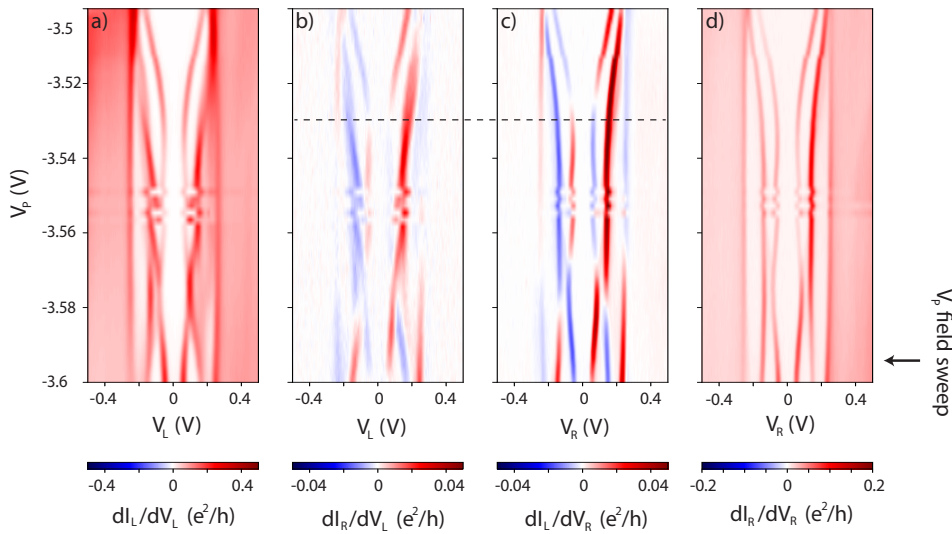


Figure 6.7: a) Local differential conductance  $dI_L/dV_L$  in dependence of Plunger potential  $V_P$  and left side bias  $V_L$  (identical to Figure 6.4a, shown for comparison). b) Nonlocal differential conductance  $dI_R/dV_L$  in dependence of Plunger potential  $V_P$  and left side bias  $V_L$  c) Nonlocal differential conductance  $dI_L/dV_R$  in dependence of Plunger potential  $V_P$  and right side bias  $V_R$  d) Local differential conductance  $dI_R/dV_R$  in dependence of Plunger potential  $V_P$  and right side bias  $V_R$  (identical to Figure 6.4b, shown for comparison)

In our measurements we observe signatures in the nonlocal conductances when on resonance with these ABS on either side. In Fig. 6.7a,d the local conductances from Figure 6.4a,b are plotted again for easier comparison and extended with the measurements of the nonlocal conductances  $dI_R/dV_L(V_L)$  and  $dI_L/dV_R(V_R)$  from the same set of data. Again, our measurement setup allows for the simultaneous measurement of these quantities. One can see that the resonances in the local conductances are accompanied by changes in the nonlocal conductances when being on resonance with the ABS. The electron and hole parts of the ABS have positive and negative signs in differential conductance which changes sign at the degeneracy point of the state. The dashed line acts as visual aid to show that the crossover point from positive to negative differential conductance happens at slightly different values of  $V_P$  for the right and left side. In a different regime we also

observe states that are not accompanied by this signature in nonlocal conductance and at the same time (maybe purely by chance) do not have a counterpart in the local conductance of the other side (see Fig. 6.8 Box). In this measurement the left side is slightly more closed than before. Another thing worth mentioning in this measurement is that the nonlocal signal is present for the subgap states but not for the coherence peaks at the border of the gap.

We measured this feature carefully in different measurement configurations to minimize the possibility of it being a measurement artifact (see Appendix). The nonlocal signatures disappear when completely pinching off the other side and when floating the lead while the local resonances stay.

We observe states with no nonlocal signature and we observe no nonlocal signal associated with the coherence peaks - so it seems this feature cannot be fully explained by voltage dividing effects as it does not strictly follow a change in the local conductances. The model provided in Section 3.4.2 reproduces these findings qualitatively and Gramich *et al.* [34] observe similar signatures in a three terminal measurement on a carbon nanotube. In the model we identify two processes, *ABS mediated tunneling* and *nonlocal CP formation*, being responsible for the two different signs in the nonlocal conductance. As these processes involve all three leads, it would explain why the state only visible on the right side in Fig. 6.8 does not carry a nonlocal conductance signature as the decoupling from one lead might lead to the vanishing of the nonlocal conductance. As both processes are proportional to two different tunneling amplitudes this would furthermore give an explanation for the asymmetry observed on the left side in Fig. 6.8 (below the box) as the process associated with the negative differential conductance seems suppressed on the left side.

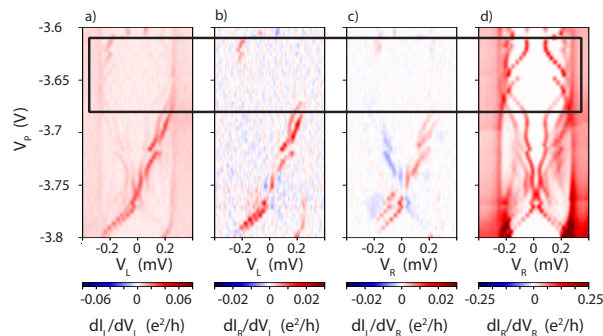


Figure 6.8: a) Local differential conductance  $dI_L/dV_L$  in dependence of plunger potential  $V_P$  and left side bias  $V_L$  (identical to Figure 6.4a, shown for comparison). b) Nonlocal differential conductance  $dI_R/dV_L$  in dependence of plunger potential  $V_P$  and left side bias  $V_L$  c) Nonlocal differential conductance  $dI_L/dV_R$  in dependence of plunger potential  $V_P$  and right side bias  $V_R$  d) Local differential conductance  $dI_R/dV_R$  in dependence of plunger potential  $V_P$  and right side bias  $V_R$  (identical to Fig. 6.4b, shown for comparison) Box highlights a subgap state which only appears in the local conductance of the right side and has no nonlocal signature.

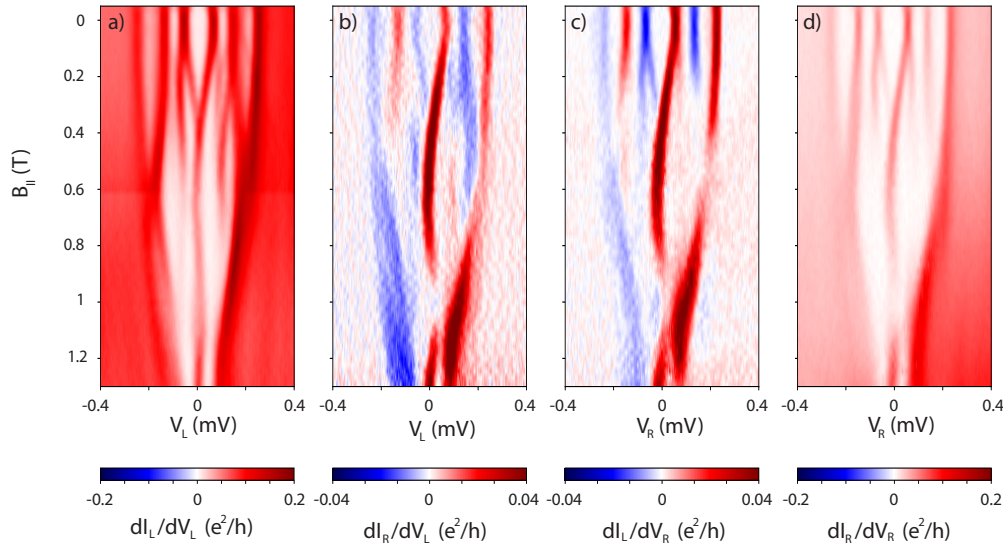


Figure 6.9: a) Local differential conductance  $dI_L/dV_L$  in dependence of parallel magnetic field  $B_{||}$  and left side bias  $V_L$  b) Nonlocal differential conductance  $dI_R/dV_L$  in dependence of parallel magnetic field  $B_{||}$  and left side bias  $V_L$  c) Nonlocal differential conductance  $dI_L/dV_R$  in dependence of parallel magnetic field  $B_{||}$  and right side bias  $V_R$  d) Local differential conductance  $dI_R/dV_R$  in dependence of parallel magnetic field  $B_{||}$  and right side bias  $V_R$

## 6.4 Field dependence

A parallel magnetic field is applied in direction of the nanowire to study the behavior of the subgap states and possibly observe a topological phase transition. The position in plunger space  $V_p$  is marked by a black arrow in Figure 6.7. The field is aligned by rotating the angle of the magnetic field around the expected direction of the nanowire from the mounting in the fridge and then settle on the angle for which the measured gap of the system is the largest. Again two sided tunnel spectroscopy is measured, where we sweep the bias on both tunneling probes individually and then step the magnetic field incrementally. The local conductances are plotted in Figure 6.9a,d. We observe two subgap states at zero field on both sides with a electron and hole like part. The state closest to zero energy splits at  $\sim 180$  mT on both sides. The outer states merges with the continuum of the closing gap at 0.6 T. The inner split part of the inner state crosses zero energy at 0.4 T and seems to stick shortly for 0.2 T, slightly deviating from zero energy and then sticking to zero energy again at 1 T. In the local conductance on the right side three subgap states fade away starting at 0.4 T. On the contrary the states persist for longer in the left local conductance and only the two outer states start to dim at 0.7 T but never fully vanish. This behavior seems correlated by eye but decreases for increasing magnetic field as some of the subgap states vanish at different magnetic fields. Unfortunately the direction of the wire and the placement of the die inside the cryostat does not allow to increase the magnetic field to high enough values to fully close the gap, so  $B_C$  stays unknown in this measurement.

Now considering the measurement of the nonlocal conductances in 6.9b,c one can ob-

serve the previously observed signatures of positive and negative differential conductance at zero field. One thing to highlight is that the sign of the negative differential conductance is being retained at the splitting of the inner states in Figure c) at 0.2 T. Another thing to notice is that all three subgap states vanishing in the right local conductance are attributed with negative differential conductance in the nonlocal picture. The two states that dim on the left side are also associated with negative differential conductance. Also at the point where the subgap states merge at 0.2 T, the positive differential conductance overrules the negative differential conductance.

It has been shown for well-separated Majorana zero modes that current flowing into/out of both MZMs is uncorrelated [56]. Since a nonlocal conductance is observed for the zero-energy states in Figure 6.9, we conclude that these features cannot be explained by well-separated Majoranas. This conclusion is perhaps unsurprising, given the short length of the device 300 nm. In other words, the mere observation of non-local conductance for zero-energy feature does not strongly distinguish between trivial Andreev bound states and Majorana precursors on this length scale. However, more nuanced analysis may provide insight as to the character of the low-energy states, even in the short-device limit. In the rate equation model the strength of the nonlocal current is proportional to the difference of the Bogoliubov de Gennes amplitudes of the ABS  $I_2 \propto (u^2 - v^2)$ . These amplitudes have predicted characteristic correlations for Majorana precursors and trivial ABS [57] so this measure in nonlocal conductance could furthermore be worked out to distinguish Majorana precursors from trivial ABS even in the short wire limit. For Majorana precursors it is predicted that the difference between  $u$  and  $v$  is maximized for when the precursor states is at zero energy and minimized with  $u = v$  when the state is the furthest separated from zero energy in the field evolution. We consider the Figure 6.9b. As the two subgap states merge at 0.4 T the nonlocal conductance is maximized at  $\sim 0.04 e^2/h$ . At the turnaround point at 0.7 T the nonlocal conductance has slightly lowered to  $\sim 0.03 e^2/h$ . When returning to zero energy at 1 T the nonlocal conductance minimizes and vanishes completely for around 0.1 T. This is inconsistent with the predictions for Majorana precursors as one would expect the nonlocal conductance to maximize at 0.4 and 1 T (as these mark the point of maximum difference between  $u$  and  $v$ ) and minimize at the turnaround point at 0.7 T as  $u \sim v$ . A more thorough analysis on more observed field evolutions of different states is necessary to draw further conclusions.

If this nonlocal conductance signature really is associated with ABS extending over the whole length of the wire, the nonlocal conductance could possibly be used as a criterion in the long wire limit to distinguish topological phase transitions from trivial, extended ABS. Well separated MZMs should not show this signature in nonlocal conductance.

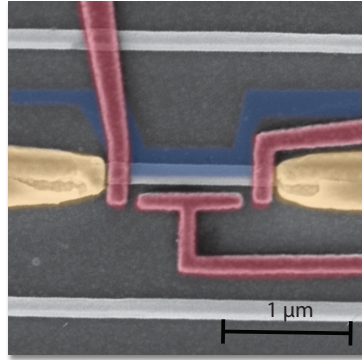


Figure 6.10: 1  $\mu\text{m}$  long three terminal device with two normal leads (yellow) and one superconducting lead (blue), two gates to create tunneling barriers and one gate to tune barrier (red). The superconducting lead is split to be allow for separate applied current and voltage drop measurement.

## 6.5 Possible Majorana zero modes

We switch our attention to a similar device with two normal leads and one superconducting lead on another die (Figure 6.10). The SAG wafer is grown by the Manfra group from Purdue University in an MBE: On a GaAs substrate capped with SiO an InGaAs buffer is grown and then topped by InAs. The die is covered in situ by 7 nm of Al. The fabrication procedure is similar to the one previously described altering slightly in EBL doses because of different backscattering properties of GaAs over InP and etching parameters because of different Al thickness. The measurement setup is identical as previously described. The device is tuned into the tunneling regime on both sides and a parallel magnetic field is applied from 0 to 1 T. In 6.11a,b the two local conductances on the left and right side are plotted in dependence of left/right side bias  $V_{L/R}$  and applied parallel magnetic field  $B_{||}$ . On the right tunneling barrier we observe two subgap states coming down in field and merging at 0.4 T. They stick for 200 mT when more subgap states converging to zero energy hide the feature but we can not observe it moving away from zero energy up to 1T. The superconducting gap is still partly open up to 1 T. We refer to this feature as a zero bias peak. On the contrary on the left side one can also observe subgap states converging to zero energy but they merge already at 0.3 T and do not seem to stick to zero energy. More subgap states come down to zero energy up to 1 T and make it hard to tell what exactly is going on in this regime.

We further study the dependency of this one sided zero bias peak in gate dependence. The local conductances on the left and right side are plotted in dependence of left/right side bias  $V_{L/R}$  and gate potential  $V_p$  in Figure 6.11c,d at 0.45 T. This is marked in the field sweep as a black arrow . The position of the field sweep in  $V_p$  is also indicated by a black arrow. Cuts are taken at the colored dashed lines and plotted in Figure 6.12. We observe a clearly defined gap on the right side with a subgap state sitting at zero energy between -0.08 and -0.03  $V_p$ . Unfortunately we do not observe coulomb peaks in these devices so

there is no easy way to extract the *lever arm*, which would relate energy of the states to the voltage on the gates. On the left side we see a superconducting gap with a variety of subgap states but not one of them seems to converge to zero energy at the interval of  $V_P$  we observe the other zero bias state in. This zero bias peak may or may not be related to a topological

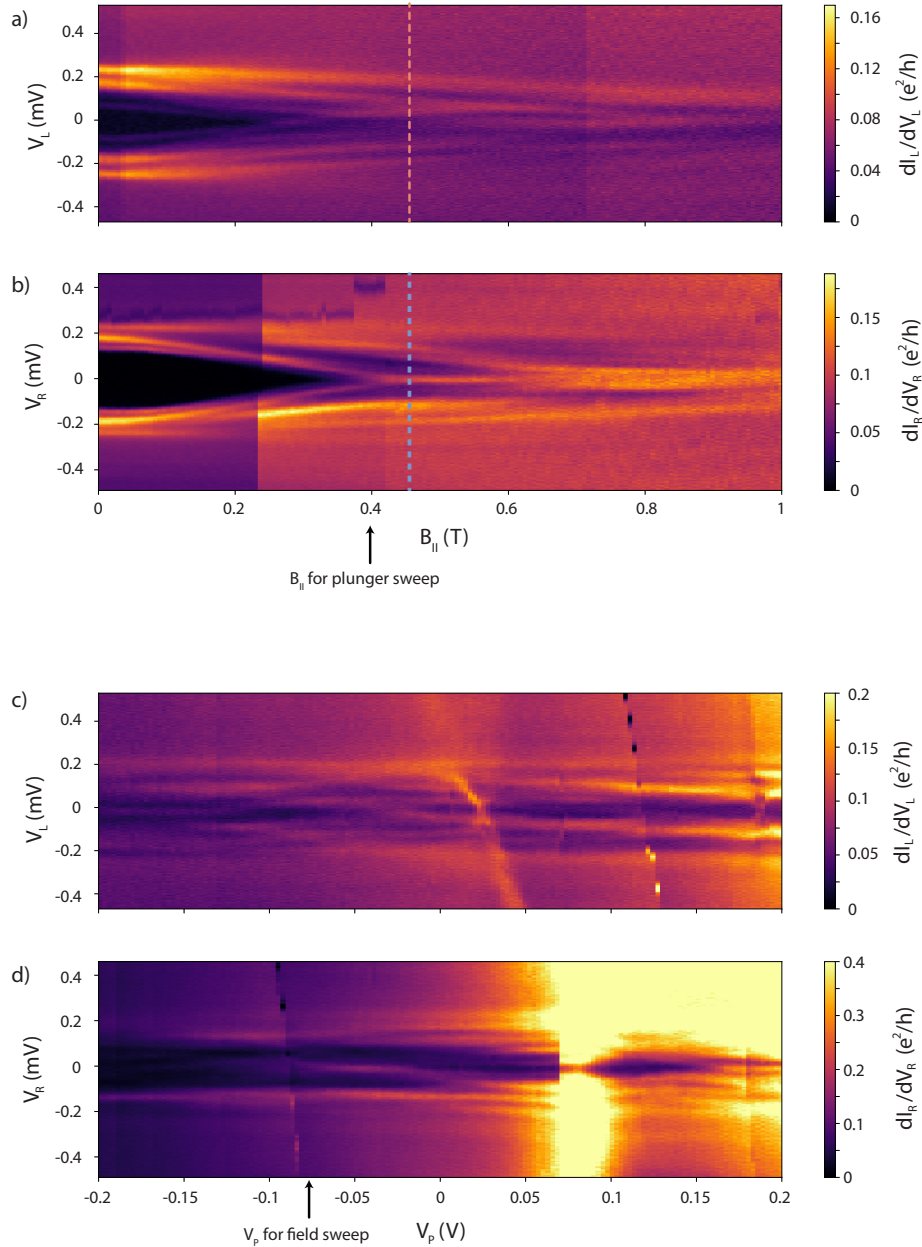


Figure 6.11: a) Local differential conductance  $dI_L/dV_L$  in dependence of parallel magnetic field  $B_{||}$  and left side bias  $V_L$  b) Nonlocal differential conductance  $dI_R/dV_L$  in dependence of parallel magnetic field  $B_{||}$  and right side bias  $V_R$  , c) Local differential conductance  $dI_L/dV_L$  in dependence of density tuning  $V_P$  and left side bias  $V_L$  at 0.4 T d) Nonlocal differential conductance  $dI_R/dV_L$  in dependence of density tuning  $V_P$  and right side bias  $V_R$

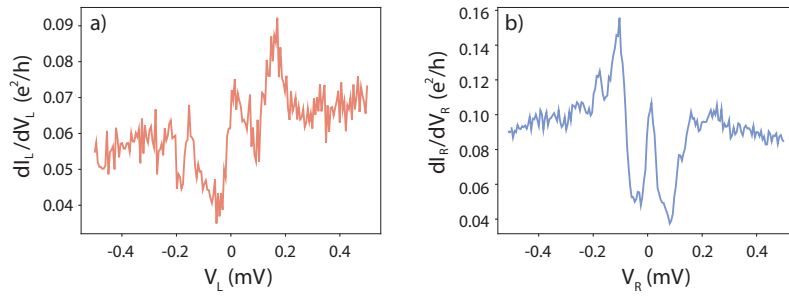


Figure 6.12: Cuts taken at the colored dashed lines in Figure 6.11

phase transition. As this wire is longer than one previously discussed the separation of possible Majorana zero modes is higher and hybridization which would cause an oscillation around zero energy is reduced [55]. The zero bias feature might also be caused by some Andreev bound states present in the system masking themselves as a Majorana zero mode signature. If it is indeed a topological phase transition, it would lose topological protection as soon as the excited states converge to zero energy at 0.6-0.7 T. In any case, the possible topological phase or the ABS does not extend to the other side of the wire. This is probably caused by disorder in the wire or by a suboptimal interface between the superconductor and semiconductor which would create parts of the wire which are not proximitized and do not possess a superconducting gap. This creates potential barriers/wells which would create two or more distinct parts of the wire.

## 7 Conclusion and Outlook

### 7.1 Conclusion

By using selective area grown structures as a new platform for the search for Majorana quasiparticles we extend the classical two terminal nanowire geometries to three terminals. Fabrication, measurement setup and tools and complications arising from this third terminal are discussed. The experimental data are shown from a three terminal device with two normal lead and one superconducting lead made from epitaxial aluminum. By performing simultaneous two sided tunneling spectroscopy we observe a variety of Andreev bound states in the local conductances which seem to be correlated in a device with 300nm between tunneling probes. We show that some of these states are more strongly coupled to one of the two leads with additional slightly different behaviors like avoided crossings on one of the two sides. In comparison to the same measurement on a device where the separation extends to 900nm we show that these correlations are not visible over this length and strengthen this argument by extracting correlation histograms from the measurement data sets. We interpret this missing correlation as an upper boundary for the superconducting coherence length of our hybrid system. The shorter system seems to be in the  $L/2 < \xi$  regime while the long device extends to the  $L/2 > \xi$ . The missing correlations on the long device also rule out voltage division as a cause for these correlations as it possesses the same resistive network as the short device.

By measuring the nonlocal conductance in the same measurement, we find that these Andreev bound states can be associated with an additional signature in nonlocal differential conductance which changes its sign at electron hole degeneracy point of the ABS. We find a state that does not show this behavior in nonlocal conductance. It happens to not possess a correlated state on the other side. We rule out voltage division effects as a cause for this behavior and find a possible interpretation which reproduces these findings in nonlocal conductance qualitatively [34]. The sign change of the nonlocal differential conductance is interpreted as two different processes: one being an ABS mediated transport from one normal lead to the other while the other represents the nonlocal formation/splitting of a Cooper pair. Furthermore we study the behavior of these ABS in parallel magnetic field and search for a topological phase transition in this system. While we find an ABS converging to zero energy we do not find conclusive evidence for a topological phase forming in our system. We observe ABS associated with negative differential conductance in the nonlocal conductance vanishing at higher fields which we interpret as some sort of spin blockade arising and preventing tunneling spectroscopy into this part of the ABS.

In a third device of similar geometry with a length of 1  $\mu\text{m}$  of a different growth we observe the first zero bias conductance peak in this new material on one side of our device. It sticks to zero energy in magnetic field over 300 mT before it merges with excited states. It stays at zero energy in gate potential with unknown lever arm. We interpret this zero bias peak as a possible topological phase transition which does not seem to extend over the whole length of the wire, as the other tunneling probe does not see the same signature and observes a different density of states. We identify disorder in the wire as a possible cause.

## 7.2 Outlook

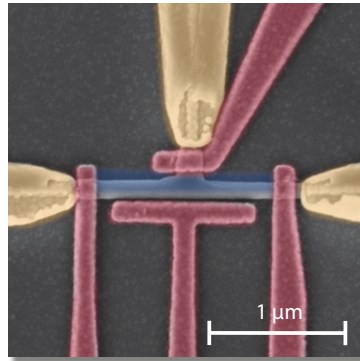


Figure 7.1: Three terminal device with three normal leads and three tunneling probes which allow to form an island

The topic of topological quantum computing is a promising approach to a full, true scalable quantum computer. Selective area grown nanowire networks as a platform develop as a promising candidate to host these non-abelian excitation. In this work we only used one of the advantages of SAG over VLS nanowires - the in situ deposited superconducting plane covering the die. To fully utilize the nanowire networks that can be grown on this platform will be the task of coming experiments (Figure 7.1 shows a semiconducting T-device from one of the fabricated dies in this work). As it is still new material and optimal growth parameters and composition of the structures have to be worked out, material quality will increase in the near future. The work in this thesis should be viewed as a framework to investigate possible topological phase transitions by providing more evidence than the one-sided zero bias peak in differential conductance. By being able to measure the tunneling processes into both possible Majorana zero modes on both ends of the wire and extracting correlations of their behavior in parallel magnetic field and electric field one gains additional information into the extent of the topological phase. The non-local conductance also allows a peak of the properties of the bulk not probed by the local tunneling spectroscopy [52] and has predicted signatures for topological phase transition which would allow to separate trivial zero bias peaks caused by ABS from Majorana zero modes. The zero bias conductance peak on one side showed here should be viewed as a promising first step and future experiments will study this behavior at different separation length of the tunneling probes. As quality of material improves the next step would be a correlated zero bias peak present in the density of states on both sides, indicating that the material would be ready for more sophisticated experiments like a Majorana interferometer [50] or a braiding experiment showing the non-abelian statistic of these excitations [58]. A roadmap to a topological qubit is visible.

## References

- [1] Sami Franssila. *Introduction to microfabrication*. John Wiley & Sons, 2010.
- [2] G. E. Moore. Cramming More Components onto Integrated Circuits. *Electronics*, 38(8):114–117, April 1965.
- [3] T. N. Theis and H. S. P. Wong. The end of moore’s law: A new beginning for information technology. *Computing in Science Engineering*, 19(2):41–50, Mar 2017.
- [4] Richard P Feynman. Quantum mechanical computers. *Foundations of physics*, 16(6):507–531, 1986.
- [5] D. Deutsch and R. Jozsa. Rapid solution of problems by quantum computation. *Proceedings of the Royal Society of London A: Mathematical, Physical and Engineering Sciences*, 439(1907):553–558, 1992.
- [6] P. Shor. Polynomial-time algorithms for prime factorization and discrete logarithms on a quantum computer. *SIAM Journal on Computing*, 26(5):1484–1509, 1997.
- [7] Lov K. Grover. A fast quantum mechanical algorithm for database search. In *Proceedings of the Twenty-eighth Annual ACM Symposium on Theory of Computing*, STOC ’96, pages 212–219, New York, NY, USA, 1996. ACM.
- [8] David P. DiVincenzo and IBM . The physical implementation of quantum computation. 48, 03 2000.
- [9] Michael A Nielsen and Isaac L Chuang. *Quantum computation and quantum information*, 2000.
- [10] Barbara M Terhal. Quantum error correction for quantum memories. *Reviews of Modern Physics*, 87(2):307, 2015.
- [11] Markus J Storcz and Frank K Wilhelm. Decoherence and gate performance of coupled solid-state qubits. *Physical Review A*, 67(4):042319, 2003.
- [12] Andrew A Houck, Jens Koch, Michel H Devoret, Steven M Girvin, and Robert J Schoelkopf. Life after charge noise: recent results with transmon qubits. *Quantum Information Processing*, 8(2-3):105–115, 2009.
- [13] Martin Leijnse and K Flensberg. Introduction to topological superconductivity and majorana fermions. 27, 06 2012.
- [14] J. M. Kosterlitz and D. J. Thouless. Ordering, metastability and phase transitions in two-dimensional systems. *Journal of Physics C Solid State Physics*, 6:1181–1203, April 1973.
- [15] D. Hsieh, D. Qian, L. Wray, Y. Xia, Y. S. Hor, R. J. Cava, and M. Z. Hasan. A topological dirac insulator in a quantum spin hall phase. *Nature*, 452:970 EP –, Apr 2008.
- [16] David Hsieh, Yuqi Xia, L Wray, Dong Qian, Arijeet Pal, JH Dil, J Osterwalder, F Meier, G Bihlmayer, CL Kane, et al. Observation of unconventional quantum spin textures in topological insulators. *Science*, 323(5916):919–922, 2009.

- [17] Roman M Lutchyn, Jay D Sau, and S Das Sarma. Majorana fermions and a topological phase transition in semiconductor-superconductor heterostructures. *Physical review letters*, 105(7):077001, 2010.
- [18] Chetan Nayak, Steven H Simon, Ady Stern, Michael Freedman, and Sankar Das Sarma. Non-abelian anyons and topological quantum computation. *Reviews of Modern Physics*, 80(3):1083, 2008.
- [19] Michael Freedman, Alexei Kitaev, Michael Larsen, and Zhenghan Wang. Topological quantum computation. *Bulletin of the American Mathematical Society*, 40(1):31–38, 2003.
- [20] Ady Stern and Bertrand I Halperin. Proposed experiments to probe the non-abelian  $\nu=5/2$  quantum hall state. *Physical review letters*, 96(1):016802, 2006.
- [21] Parsa Bonderson, Alexei Kitaev, and Kirill Shtengel. Detecting non-abelian statistics in the  $\nu=5/2$  fractional quantum hall state. *Physical review letters*, 96(1):016803, 2006.
- [22] Xie Chen, Lukasz Fidkowski, and Ashvin Vishwanath. Symmetry enforced non-abelian topological order at the surface of a topological insulator. *Physical Review B*, 89(16):165132, 2014.
- [23] H. K. Onnes. The resistance of pure mercury at helium temperatures. *Commun. Phys. Lab. Univ. Leiden*, 12:120+, 1911.
- [24] J. Bardeen, L. N. Cooper, and J. R. Schrieffer. Theory of superconductivity. *Phys. Rev.*, 108:1175–1204, Dec 1957.
- [25] Philip Phillips. *Advanced solid state physics*. Cambridge Univ. Press, Cambridge [u.a.], 2. ed. edition, 2012.
- [26] M. Tinkham. *Introduction to Superconductivity: Second Edition*. Dover Books on Physics. Dover Publications, 2004.
- [27] AF Andreev. The thermal conductivity of the intermediate state in superconductors. *Sov. Phys. JETP* 19, 46(5):1823–1828, 1964.
- [28] P. G. de Gennes and D. Saint-James. Elementary excitations in the vicinity of a normal metal-superconducting metal contact. *Physics Letters*, 4:151–152, March 1963.
- [29] D Saint-James. Excitations élémentaires au voisinage de la surface de séparation d’un métal normal et d’un métal supraconducteur. *Journal de Physique*, 25(10):899–905, 1964.
- [30] K. Neurohr, A. A. Golubov, Th. Klocke, J. Kaufmann, Th. Schäpers, J. Appenzeller, D. Uhlisch, A. V. Ustinov, M. Hollfelder, H. Lüth, and A. I. Braginski. Properties of lateral nb contacts to a two-dimensional electron gas in an  $\text{in}_{0.77}\text{ga}_{0.23}\text{as}/\text{inp}$  heterostructure. *Phys. Rev. B*, 54:17018–17028, Dec 1996.
- [31] Jean-Damien Pillet. *Tunneling spectroscopy of the Andreev Bound States in a Carbon Nanotube*. PhD thesis, Université Pierre et Marie Curie-Paris VI, 2011.

- 
- [32] J. A. Sauls. Andreev bound states and their signatures. *Philosophical Transactions of the Royal Society of London A: Mathematical, Physical and Engineering Sciences*, 376(2125), 2018.
- [33] Eduardo JH Lee, Xiaocheng Jiang, Manuel Houzet, Ramon Aguado, Charles M Lieber, and Silvano De Franceschi. Spin-resolved andreev levels and parity crossings in hybrid superconductor–semiconductor nanostructures. *Nature nanotechnology*, 9(1):79, 2014.
- [34] J. Gramich, A. Baumgartner, and C. Schönenberger. Andreev bound states probed in three-terminal quantum dots. *Phys. Rev. B*, 96:195418, Nov 2017.
- [35] Eduardo J. H. Lee, Xiaocheng Jiang, Manuel Houzet, Ramón Aguado, Charles M. Lieber, and Silvano De Franceschi. Spin-resolved andreev levels and parity crossings in hybrid superconductor-semiconductor nanostructures. *Nature Nanotechnology*, 9:79 EP –, Dec 2013. Article.
- [36] Tobias Meng, Serge Florens, and Pascal Simon. Self-consistent description of andreev bound states in josephson quantum dot devices. *Physical Review B*, 79(22):224521, 2009.
- [37] A Yu Kitaev. Unpaired majorana fermions in quantum wires. *Physics-Uspeski*, 44(10S):131, 2001.
- [38] Yuval Oreg, Gil Refael, and Felix von Oppen. Helical liquids and majorana bound states in quantum wires. *Physical review letters*, 105(17):177002, 2010.
- [39] Graham Kells, Dganit Meidan, and PW Brouwer. Near-zero-energy end states in topologically trivial spin-orbit coupled superconducting nanowires with a smooth confinement. *Physical Review B*, 86(10):100503, 2012.
- [40] Chun-Xiao Liu, Jay D Sau, Tudor D Stanescu, and S Das Sarma. Andreev bound states versus majorana bound states in quantum dot-nanowire-superconductor hybrid structures: Trivial versus topological zero-bias conductance peaks. *Physical Review B*, 96(7):075161, 2017.
- [41] Vincent Mourik, Kun Zuo, Sergey M Frolov, SR Plissard, Erik PAM Bakkers, and Leo P Kouwenhoven. Signatures of majorana fermions in hybrid superconductor-semiconductor nanowire devices. *Science*, 336(6084):1003–1007, 2012.
- [42] M. T. Deng, S. Vaitiekenas, E. B. Hansen, J. Danon, M. Leijnse, K. Flensberg, J. Nygård, P. Krogstrup, and C. M. Marcus. Majorana bound state in a coupled quantum-dot hybrid-nanowire system. *Science*, 354(6319):1557–1562, 2016.
- [43] Fabrizio Nichele, Asbjørn C. C. Drachmann, Alexander M. Whiticar, Eoin C. T. O’Farrell, Henri J. Suominen, Antonio Fornieri, Tian Wang, Geoffrey C. Gardner, Candice Thomas, Anthony T. Hatke, Peter Krogstrup, Michael J. Manfra, Karsten Flensberg, and Charles M. Marcus. Scaling of majorana zero-bias conductance peaks. *Phys. Rev. Lett.*, 119:136803, Sep 2017.

- 
- [44] Torsten Karzig, Christina Knapp, Roman M. Lutchyn, Parsa Bonderson, Matthew B. Hastings, Chetan Nayak, Jason Alicea, Karsten Flensberg, Stephan Plugge, Yuval Oreg, Charles M. Marcus, and Michael H. Freedman. Scalable designs for quasiparticle-poisoning-protected topological quantum computation with majorana zero modes. *Phys. Rev. B*, 95:235305, Jun 2017.
- [45] P Krogstrup, NLB Ziino, W Chang, SM Albrecht, MH Madsen, Erik Johnson, Jesper Nygård, CM Marcus, and TS Jespersen. Epitaxy of semiconductor–superconductor nanowires. *Nature materials*, 14(4):400, 2015.
- [46] Filip Krizek. Private conversation. 2018.
- [47] Filip Krizek, Joachim Elbeshausen Sestoft, Pavel Aseev, Sara Martí-Sánchez, Saulius Vaitiekėnas, Lucas Casparis, Sabbir A. Khan, Yu Liu, Tomaš Stankevič, Alexander M. Whiticar, Alexandra Fursina, Frenk Boekhout, Rene Koops, Emanuele Uccelli, Leo P. Kouwenhoven, Charles Marcus, Jordi Arbiol, and Peter Krogstrup. Scalable quantum nanowire networks grown by molecular beam epitaxy. 02 2018.
- [48] Blue Fors. Bf-xld-series manual version 1.5.0. 2016.
- [49] Frank Pobell. *Matter and methods at low temperatures*, volume 2. Springer, 1996.
- [50] AR Akhmerov, Ar akhmerov, j. nilsson, and cwj beenakker, phys. rev. lett. 102, 216404 (2009). *Phys. Rev. Lett.*, 102:216404, 2009.
- [51] GE Blonder, M Tinkham, and TM Klapwijk. Transition from metallic to tunneling regimes in superconducting microconstrictions: Excess current, charge imbalance, and supercurrent conversion. *Physical Review B*, 25(7):4515, 1982.
- [52] TÖ Rosdahl, A Vuik, M Kjaergaard, and AR Akhmerov. Andreev rectifier: A non-local conductance signature of topological phase transitions. *Physical Review B*, 97(4):045421, 2018.
- [53] Guy Deutscher and Denis Feinberg. Coupling superconducting-ferromagnetic point contacts by andreev reflections. *Applied Physics Letters*, 76(4):487–489, 2000.
- [54] Anindya Das, Yuval Ronen, Moty Heiblum, Diana Mahalu, Andrey V Kretinin, and Hadas Shtrikman. High-efficiency cooper pair splitting demonstrated by two-particle conductance resonance and positive noise cross-correlation. *Nature communications*, 3:1165, 2012.
- [55] Tudor D Stanescu, Roman M Lutchyn, and S Das Sarma. Dimensional crossover in spin-orbit-coupled semiconductor nanowires with induced superconducting pairing. *Physical Review B*, 87(9):094518, 2013.
- [56] CJ Bolech and Eugene Demler. Observing majorana bound states in p-wave superconductors using noise measurements in tunneling experiments. *Physical review letters*, 98(23):237002, 2007.
- [57] Esben Bork Hansen, Jeroen Danon, and Karsten Flensberg. Probing electron-hole components of subgap states in coulomb blockaded majorana islands. *Physical Review B*, 97(4):041411, 2018.

- [58] David Aasen, Michael Hell, Ryan V Mishmash, Andrew Higginbotham, Jeroen Danon, Martin Leijnse, Thomas S Jespersen, Joshua A Folk, Charles M Marcus, Karsten Flensberg, et al. Milestones toward majorana-based quantum computing. *Physical Review X*, 6(3):031016, 2016.

## A Single bias vs. dual biasing

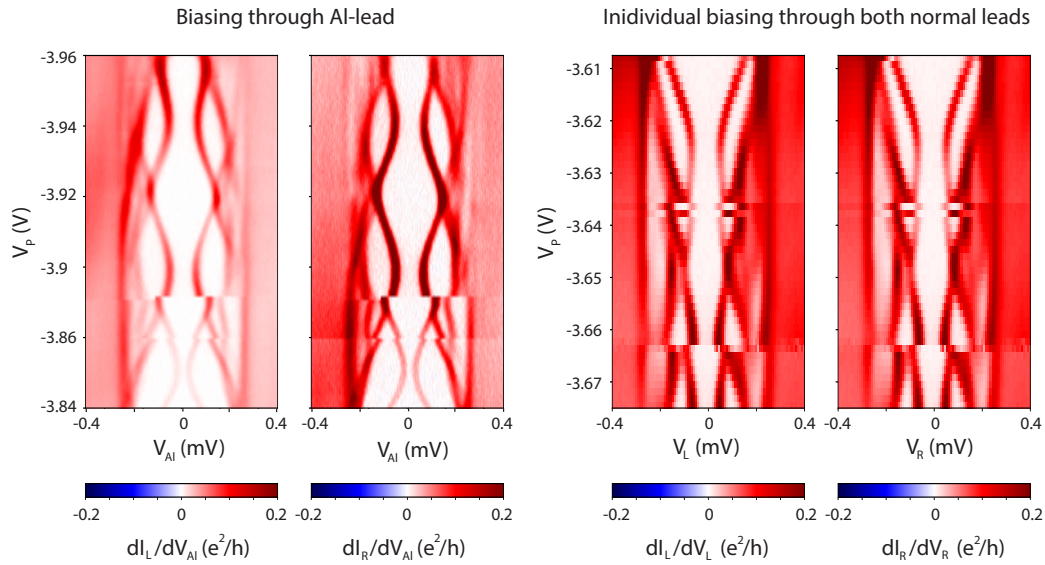


Figure A.1: Left: Local conductances with one AC excitation and DC bias applied to the superconducting lead. Right: Local conductances with an AC excitation and DC bias applied to each normal lead - individual biasing.

This section shortly compares the two local conductances measured in both measurement setups mentioned in this thesis. In Figure A.1a,b there is only one AC and DC excitation applied to the superconducting lead while in c,d the described setup with dual biasing on both normal leads is used in a similar but slightly different regime of  $V_p$  in the 300nm device. In both measurement setups the two sides are correlated by eye and very comparable indicating that for local conductances both measurement setups are valid to record data. The single biasing setup does not allow for the measurement of the nonlocal conductances and the full conductance picture but allows for faster data acquisition as only one DC bias is swept.

## B Voltage division effects

As the nonlocal signal observed in Chapter 6.3 was not expected we were very wary of it being a measurement artifact. On top of that correlations between the two leads could be induced simply by a resistive network and not ongoing processes in our samples. In this chapter we shortly presents measurements we did to increase our confidence that we are observing a real phenomenon.

### B.1 Floating third lead

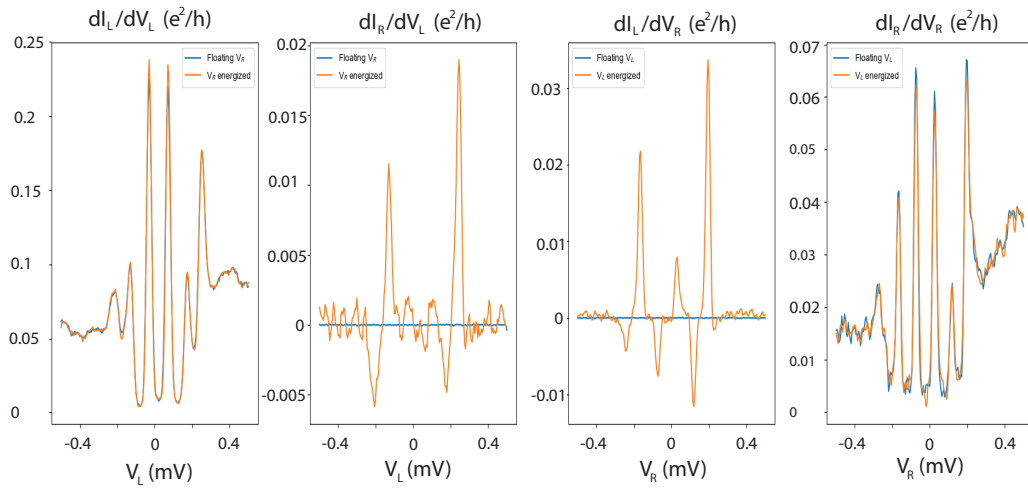


Figure B.1: Conductance measured with the third lead floating (blue)/ non floating (yellow) to show correlations are not induced on both sides through voltage division effects. From left to right:  $dI_L/dV_L(V_L)$ ,  $dI_R/dV_L(V_L)$ ,  $dI_L/dV_R(V_R)$ ,  $dI_L/dV_R(V_R)$  and  $dI_R/dV_R(V_R)$ .

In this measurement we compare two sided tunnel spectroscopy with one sided tunneling spectroscopy with the second normal lead grounded (Figure B.1). Grounding the third lead transforms our measurement into the two terminal regime with no voltage divider present. As one can see, the density of states observed in the local conductances  $dI_L/dV_L$  (a) and  $dI_R/dV_R$  (d) show very similar behavior when floating the opposite lead. This affirms that correlations on both sides are not induced by voltage division effects and rather are a property of the device. This is also strengthened through the lack of correlations in longer devices, which possess the same resistive network and only differ in the length of the tunneling probe separation. Nonlocal conductances vanish when floating the third lead which is expected as measurement on the floating lead is no longer possible.

## B.2 Differential conductance vs. derivated conductance

We first perform a measurement described as before with standard lock-in techniques. To exclude the possibility of the AC-excitation causing these signatures in nonlocal conductances, we measured the density of states with the AC-excitation turned off and only sweeping bias B.2. In this configuration, we can only measure total currents  $I_L$  and  $I_R$  with a DMM and derive  $dI_L/dV_L$  and  $dI_R/dV_R$  digitally after the measurement.

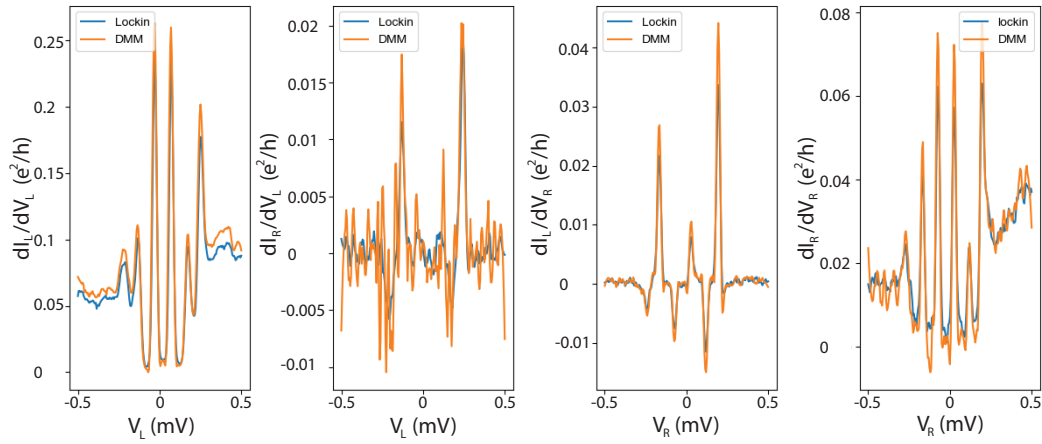


Figure B.2: Conductance measured with standard lock-in techniques as in all measurements before (blue) plotted against total current with no AC-excitations present measured with a DMM derivated digitally after measurement (yellow). From left to right:  $dI_L/dV_L(V_L)$ ,  $dI_R/dV_L(V_L)$ ,  $dI_L/dV_R(V_R)$  and  $dI_R/dV_R(V_R)$ .

### B.3 Frequency swap and all measured conductances

For further evidence, this measurement shows that swap the two excitation frequencies on the two normal lead does not lead to a qualitative difference in measurement. This shows also all eight conductances measured in our measurements.

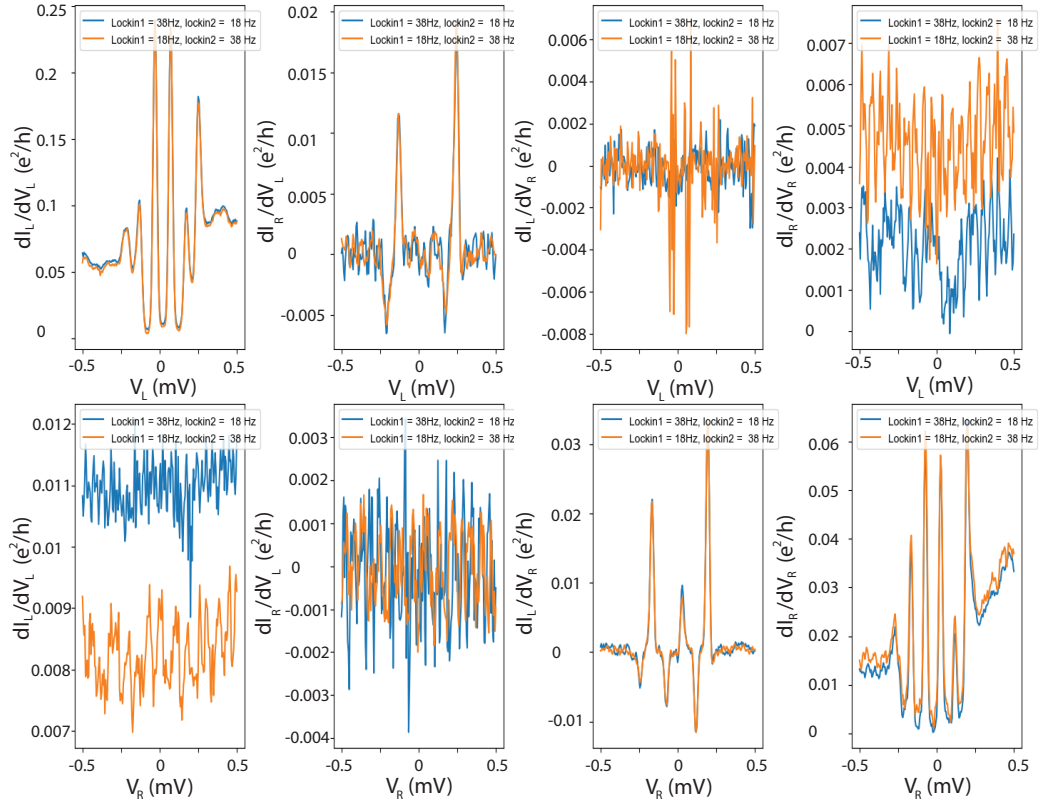


Figure B.3: All eight conductances measured with excitations frequencies used in our measurement (blue) and exchanged with each other (yellow) Top row from left to right:  $dI_L/dV_L(V_L)$ ,  $dI_R/dV_L(V_L)$ ,  $dI_L/dV_R(V_L)$  and  $dI_R/dV_R(V_L)$ . Bottom row from left to right:  $dI_L/dV_L(V_R)$ ,  $dI_R/dV_L(V_R)$ ,  $dI_L/dV_R(V_R)$  and  $dI_R/dV_R(V_R)$ .